ROYAL SOCIETY OF CHEMISTRY

REVIEW

Research progress on near-infrared long persistent phosphor materials in biomedical applications

Yan Liu, [ID] [a] Zengxue Wang,[a] Kun Miao,[a] Xundi Zhang,[a] Wei Li,[a] Pan Zhao,[a] Peng Sun,[b] Tingting Zheng, [ID] *[a] Xiuyun Zhang*[a] and Chen Chen [ID] *[c]

After excitation is stopped, long persistent phosphor materials (LPPs) can emit light for a long time. The most important feature is that it allows the separation of excitation and emission in time. Therefore, it plays a vital role in various fields such as data storage, information technology, and biomedicine. Owing to the unique mechanism of storage and luminescence, LPPs can avoid the interference of sample autofluorescence, as well as show strong tissue penetration ability, good afterglow performance, and rich spectral information in the near-infrared (NIR) region, which provides a broad prospect for the application of NIR LPPs in the field of biomedicine. In recent years, the development and applications in biomedical fields have been advanced significantly, such as biological imaging, sensing detection, and surgical guidance. In this review, we focus on the synthesis methods and luminescence mechanisms of different types of NIR LPPs, as well as their applications in bioimaging, biosensing detection, and cancer treatment in the field of biomedicine. Finally, future prospects and challenges of NIR LPPs in biomedical applications are also discussed.

1. Introduction

After the excitation using special light waves (UV, visible light, X-ray, etc., process ①), the excitation source energy stored in crystal defects is gradually released from LPPs in the form of photons (process ②), which can emit light for minutes, hours, or even longer (Fig. 1).[1–4] In China, the phenomenon of long afterglow can be traced back to the Song Dynasty, which has a history of thousands of years.[5,6] In Western countries, the first mention of such luminescent materials was in the early 17th century. When smelting gold from ore, an Italian shoemaker discovered a material that was glowing red at night. Following further investigations, the luminescence was found to be due to the presence of barium sulfide in the ore. After roasting, it was revealed that the ore could be largely transformed into barium sulfide, which is a long-lasting luminous substance. However, the afterglow performance of LPPs is currently weak, which limits the development of applications.[5] At the end of the twentieth century, Matsuzawa reported $SrAl_2O_4$:Eu^{2+}, Dy^{3+} phosphors capable of producing quite bright and long-term phosphorescence, which piqued the interest of researchers.[7]

Thereafter, researchers began to investigate LPPs in terms of luminescence mechanism and preparation methods, eventually applying such materials to the fields of safety instructions and luminous coatings.[8] In 2007, Chermont et al.[9] used the composite $Ca_{0.2}Zn_{0.9}Mg_{0.9}Si_2O_6$:$Eu^{2+}$, Dy^{3+}, Mn^{2+} for NIR biomarker imaging and diagnosis in vivo, establishing the research precedent for LPPs in the field of biomedicine. NIR long-afterglow luminescence technology was quickly brought to the forefront of the attention of the scientific community through this pioneering work.

For the biomedical field, NIR LPPs are ideal replacements for traditional fluorescent materials. The reasons are as follows. Firstly, it allows the separation of excitation and emission in time, which completely avoids the background interference of tissue autofluorescence and scattered light. Secondly, it has high sensitivity and signal-to-noise ratio.[10,11] Finally, the NIR light region is the emission range of LPPs that has less absorption and scattering, allowing strong penetration into biological tissues and opening up a new field for biomedicine.[12] NIR light was discovered as the first invisible light. The American Society for Testing and Materials (ASTM) stipulates that its wavelength range is between 700 nm and 2500 nm. According to different wavelengths, the NIR light region is divided into region I (NIR-I, 700–1100 nm) and region II/III (NIR-II/III, 1100–2500 nm).[9,10] The majority of the reported NIR LPPs are in the NIR-I region. For example, Cr^{3+} is a satisfactory wide emission center with an emission range of 650 nm–1000 nm. In addition, Mn^{4+}, Mn^{2+}, divalent rare earth ions Eu^{2+}, Yb^{2+}, tetravalent rare earth ions Pr^{4+}, Ce^{4+}, Tb^{4+}, and other-doped LPPs are excellent

[a]Department of Pharmacy, Shandong University of Traditional Chinese Medicine, Jinan 250355, Shandong, China. E-mail: ttz10_10@163.com; zhangxiuyunsh@163.com

[b]Innovative of Chinese Medicine and Pharmacy, Shandong University of Traditional Chinese Medicine, Jinan 250355, Shandong, China

[c]Key Laboratory of New Material Research Institute, Department of Acupuncture-Moxibustion and Tuina, Shandong University of Traditional Chinese Medicine, Jinan 250355, Shandong, China. E-mail: 21129008@zju.edu.cn
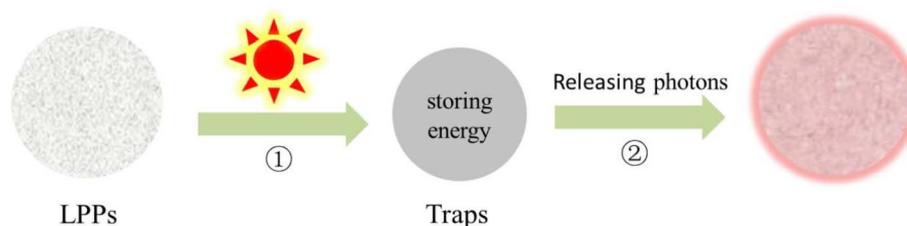
Fig. 1 Schematic diagram of LPPs luminescence.

emission centers for synthesizing NIR-I LPPs. However, only a few NIR-II/III LPPs with deeper tissue penetration and imaging contrast have been found. Some nanosized fluoride hosts ($NaYF_4$/$NaGdF_4$/$NaLuF_4$) have been reported to have long afterglow emission in the NIR-II.[13–15] For example, Zhuang et al.[13] reported monodisperse nanoscale $NaYF_4$:Ln^{3+} with narrow-band emission tunable from 480 nm to 1060 nm. The mechanism of persistent luminescence in $NaYF_4$:Ln^{3+} has been proposed through thermoluminescence measurements and a host reference binding energy (HRBE) protocol. A new 3D optical information storage application is realized, proving its application potential in anti-counterfeiting, biomedicine, and other fields. There are also some bulk hosts such as lead sulfide (PbS) quantum dots (QDs),[16] $CsPbX_3$ (X = Cl, Br, I),[17] Ba[Mg_2-Al_2N_4]:Eu^{2+}, Tm^{3+},[18] $Y_3Al_2Ga_3O_{12}$:Er^{3+}, Cr^{3+},[19] which also have NIR-II long afterglow luminescence properties. Nonetheless, NIR-II has fewer types and narrower application fields than NIR-I materials, requiring more attention. These NIR LPPs are available in data storage,[20] information technology,[21] biomedicine,[22] and other fields. Although many excellent reviews have been reported to comprehensively summarize the synthesis, luminescence mechanism, and biomedical applications of

LPPs, there are few related reviews of NIR LPPs.[23–26] Therefore, this review provides a comprehensive summary of the luminescence mechanism and synthesis methods of different types of NIR LPPs, as well as their applications in the biomedical field (Fig. 2). In addition, this paper discusses future directions and challenges.

2. Luminescence mechanism

LPPs are a class of thermoluminescent materials that emit light at room temperature, which belongs to the electron capture material.[27] The luminescence phenomenon in the electron-trapping materials is formed by the trap-level structure in the materials, such as some inorganic metal oxides, organic composites, inorganic-organic hybrids, and other LPPs. However, owing to the limited availability of analytical techniques and the complexity of the energy-level structure, there is no clear unified mechanistic model for the luminescence mechanism of this material. The currently discovered mechanisms of luminescence include the carrier transport model,[28–30] tunneling model,[31] two-photon absorption model,[32] V_k center model,[33] and displacement coordinate model.[34,35] At the same time, there is a principle called the Jablonsky diagram, which is used to explain the organic long afterglow luminescence.[36,37] Most of these luminescence mechanisms use existing band theory and other theoretical knowledge to explain the phenomena found in experiments. The following discussion mainly introduces several typical luminescence mechanism models and the main NIR LPPs.

2.1 Carrier transport model

In 1971, Abbtuscato V. et al.[38] proposed that the delayed luminescence of $SrAl_2O_4$:Eu^{2+} was caused by electron transport. It was not until 1996 that Matsuzawa et al.[7] proposed the hole transfer model, which is the first model used to explain the luminescence of $SrAl_2O_4$:Eu^{2+}, Dy^{3+}. Based on this study, Kyota Uheda et al.[39] proposed that the delayed luminescence mechanism of $ZnGa_2O_4$:Mn^{2+} is related to electron transfer and holes. The luminescence mechanism models proposed by these researchers were all about the energy transfer caused by electrons or holes. Since both electrons and holes belong to the charged particles that can move, it is recognized as the carrier transport model.[29–31]

Qu et al. investigated the red LPP of Y_2O_2S:Eu, Ti, Mg using the carrier transport model, and its luminescence mechanism
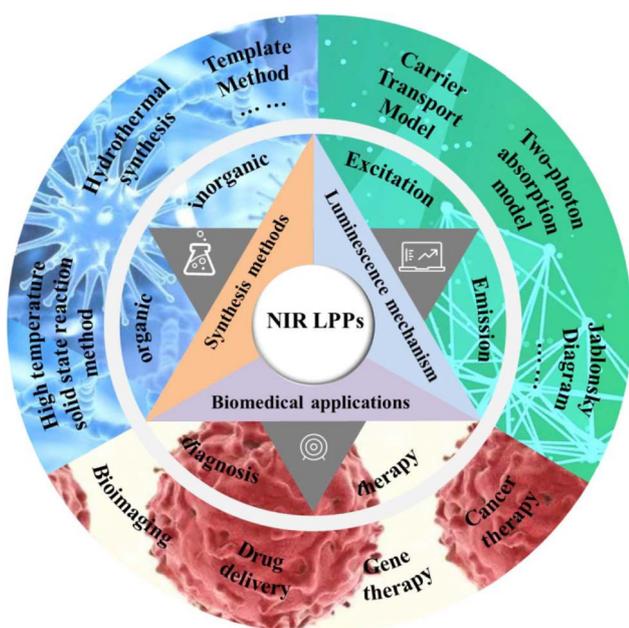

Fig. 2 Summary of the biomedical applications of NIR LPPs.

model is shown in Fig. 3a. When the luminescence center of Eu^{2+} is excited at 382 nm, the spin-level transition occurs inside the ion, and the electron transitions to the conduction band to form an electron flow (process ①). A portion of the electron flow is transformed into the excited state of Eu^{2+} and then released back to the ground state in the form of photons, resulting in yellow fluorescence (process ②). Another part of the electron flow was captured by the Ti^{4+} electron trap. When enough energy is captured, a thermal escape phenomenon will occur. The captured electrons will combine with the luminescent center of Eu^{2+}, resulting in the red afterglow phenomenon (process ③).[28]

2.2 Tunneling model

In 1958, Hougeustraten et al.[41] first discovered the tunneling model when studying sulfides, which was first used to explain the luminescence mechanism of Eu^{2+}, Dy^{2+} co-doped long afterglow materials. In 1981, Chang et al.[42] observed that there was no photoconductivity in the afterglow phenomenon of $Zn_2SiO_4:Mn^{3+}$ and $BaFBr:Eu^{2+}$ at low temperatures, which

further improved the light-emitting mechanism of the "tunneling" model. The tunneling model is separated into the full-tunneling model and the half-tunneling model. It has been discovered by researchers as a fundamental model of pyro-electric light emission. The luminescence mechanism of $KGaGeO_4:Bi^{3+}$ was investigated using a tunneling model by Sun et al.[40] A schematic diagram of its tunneling mechanism model is shown in Fig. 3b. The electron in the emitting center of Bi^{3+} is excited by UV (process ①), and Bi^{2+} is formed. At the same time, holes are generated (process ②). The holes recombine with Bi^{2+} through a tunneling process (process ③). The released energy is obtained by the Bi^{3+} emitting centers, which leap from the ground state to the excited state through the thermal escape phenomenon. Due to the non-radiative leap and specific energy-level leap, the cyan-to-blue afterglow emission phenomenon of Bi^{3+} arises (process ④).

2.3 Two-photon absorption model

The two-photon absorption model is a relatively new mechanistic model, which was proposed by Aitasalo et al.[32] when they
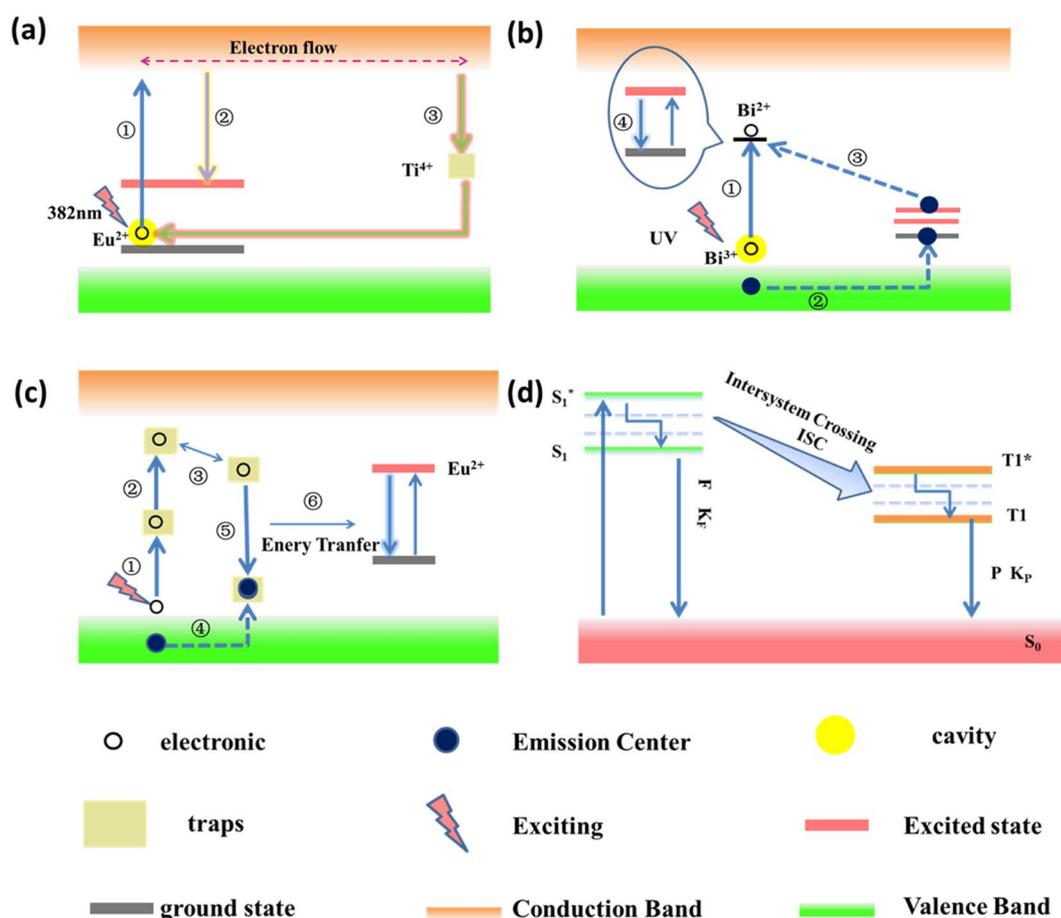
Fig. 3 Diagram of the luminescence mechanism of various materials: (a) carrier model. Reproduced from ref. 28 with permission from the Royal Society of Chemistry, copyright 2019. (b) Tunneling model. Reproduced from ref. 40 with permission from the Royal Society of Chemistry, copyright 2017. (c) Two-photon absorption model. Reproduced from ref. 32 with permission from Elsevier, copyright 2001 (d) Jablonsky diagram. Reproduced from ref. 36 with the springer nature, copyright 2019, and from ref. 37 with the springer nature, copyright 2019 (F: fluorescence. P: phosphorescence).

were studying Eu^{2+} and Dy^{3+} or Nd^{3+} co-doped aluminate systems in 2001. Fig. 3c shows a schematic diagram of the luminescence mechanism model of $CaAl_2O_4:Eu^{2+}$. Electrons in the valence band are excited to deep traps (process ①). When the energy is absorbed, they are excited to a shallow trap (process ②). Due to thermal disturbance, the electrons enter another trap (process ③). The holes in the valence band will enter the hole trap (process ④). The oxygen vacancies in the matrix are electron traps. Alkaline earth metal ion vacancies are hole traps. Electron traps capture electrons, and hole traps capture holes to form "electron–hole" pairs, which will undergo non-radiative recombination (process ⑤). Then, the energy is transferred to the Eu^{2+} luminescent center, resulting in a long afterglow phenomenon (process ⑥).[43–45]

2.4 Luminescence mechanism of organic LPPs

At present, the process of organic long afterglow luminescence is still unclear. The researchers turned to study the phenomena of luminescence in greater depth. A plausible mechanism for proposing organic-extended afterglow luminescence is based on experimental verification and related theoretical calculations. That is, the Jablonski energy-level diagram is used to explain the luminescence mechanism of organic LPPs, as

shown in Fig. 3d. When the organic molecule is excited by the external field force, it transitions from the ground state S_0 to the lowest excited state S_1. Molecules in the S_1 state are transformed into the triple excited state T_1 through the channeling between the systems. Molecules in the T_1 state are aggregated and captured by the H-aggregation, forming a stable triple-excited state. T_1^* produces long afterglow phenomena at very low radiative and nonradiative decay rates.[36,37]

2.5 Luminescence mechanism of inorganic-organic hybrid LPPs

In addition to inorganic and organic materials, researchers have hybridized the two to fully exploit the benefits of both, ushering in a new era in the field of long afterglow luminescence. As an inorganic-organic hybrid material, MOFs have the rigid porous structure of inorganic materials, and this structure can trap and stabilize the emitting molecules. Therefore, the coordination of organic fluorescent units and common metals is an effective way for MOF materials to achieve long afterglow luminescence.[46] The porous structure of MOFs contains a large number of guest molecules in their pores. There are also abundant charge-transfer processes occurring inside, which provide the possibility for a variety of luminescence pathways.
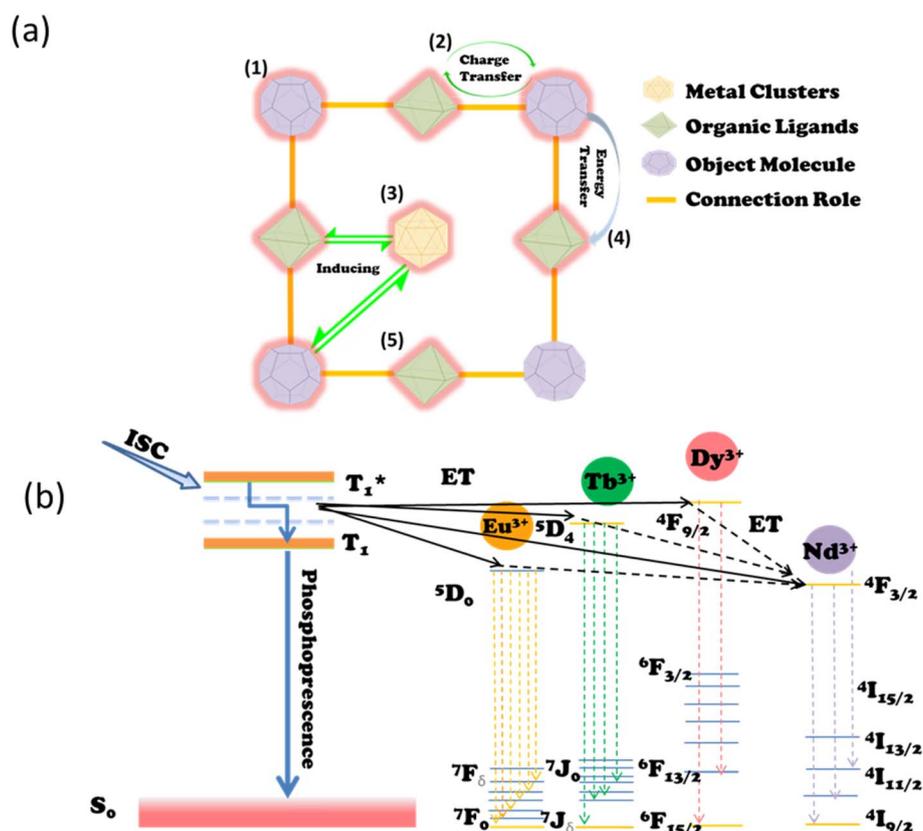
Fig. 4 (a) Multiple luminescence pathways of MOFs, including (1) metal-centered luminescence (2) metal and organic ligand-based charge transfer luminescence (3) guest-induced luminescence (4) metal and organic ligand-based transfer luminescence and (5) organic ligand-based. Reproduced from ref. 58 with permission from China national knowledge internet, copyright 2021. (b) Schematic diagram of the energy conversion between metals in LnMOFs (ISC, Intersystem Crossing; ET, Energy Transfer). Reproduced from ref. 57 with permission from the Royal Society of Chemistry, copyright 2019.

The luminescence mechanism of MOF materials is illustrated in Fig. 4a.[47–50]

Process ① is based on metal center luminescence. The luminescence mechanism mainly exists in two kinds of metal ions. One is relatively rare with d–d electron transfer of transition metal ions and s–p electron transfer of the main group of metal ions. The other is the most important lanthanide rare earth and actinide ions luminescence. It is recognized as the process of the luminescence "antenna effect". This effect usually selects for the introduction of organic molecules with chromophoric groups and chelation of rare earth ions. The process of sensitizing rare earth ions is through the energy absorbed by organic molecules, thereby emitting light.[51,52] Process ③ is guest-induced luminescence. It is mainly to endow MOFs with new luminescence ability by utilizing the permanent regular pores or pore properties of the material. We usually exchange or replace some chromophore molecules, rare earth ions, quantum dots, and other materials with strong luminescent properties into these pores. Such a luminescence mechanism conferred by the exchange of the guest is called guest-induced luminescence.[53–55] Process ⑤ is the luminescence process of organic ligands, which is the same as the luminescence process of organic long afterglow luminescent materials. The difference is that the stability and rigidity of the organic ligands increase. Processes ② and ④ are based on metal-to-organic ligand luminescence and metal-to-metal energy transfer luminescence processes. The former is based on charge transfer luminescence. It has two typical luminescence modes: charge transfer luminescence from metal to organic ligand (MLCT) and charge transfer luminescence from organic ligand to metal (LMCT).[56] The latter is based on energy transfer between metals to emit light. It is not only limited to single-metal MOF materials but has gradually expanded to the study of MOF materials containing multiple metals, especially heterometallic organic framework materials (HMOFs) and multi-metal hybrid MOF materials. The primary distinction between these two materials is that the different metal ions in HMOF have different coordination environments and coordination modes, and their crystal structures change. In contrast, mixed metal ions in multi-metal hybrid materials, typically, only, partially replace the original metal ions, while the coordination environment and coordination mode remain unchanged, resulting in crystal structures that are frequently identical to those of pure metal materials. Therefore, researchers agree that the multi-metal mixed MOF materials are more conducive to the study of the energy transfer luminescence mechanism between the metal and the metal. Zeng et al.[57] designed novel bimetallic lanthanide metal–organic framework materials (Ln-MOFs) with luminescent colors systematically investigated by energy transfer from visible light-emitting M^{3+} to NIR emitting Nd^{3+}-doped in $M_{1-x}Nd_xL_2$ for color tuning. Color tuning was investigated by doping $M_{1-x}Nd_xL_2$ with Nd^{3+} emitted in the NIR. The doping of Eu^{3+}, Tb^{3+}, or Dy^{3+} MOFs to form NIR and visible luminescence bimetallic Ln-MOFs opens up a new direction, the applied NIR spectral emission of bimetallic Ln-MOFs provides convenient applications in the field of future optical imaging. A schematic diagram of the metal-to-metal energy transfer luminescence of the Ln-MOFs is shown in Fig. 4b.

2.6 Main NIR LPPs

It is well known that the afterglow characteristics of LPPs mainly depend on the trap center and the emission center. The former is used to store energy from excitation light sources, the latter is used to emit energy after excitation has ceased.[59] Obviously, it is pretty significant to consider suitable NIR luminescence centers and traps for designing and synthesizing suitable NIR LPPs. The main matrix of LPPs contains sulfide, aluminate, silicate, gallate, germanate, titanate, and so on. Doping ions are generally introduced as luminescent centers or co-activators to improve the afterglow properties of the host. These doping ions are either rare earth ions (Eu^{2+}, Tb^{3+}, Nd^{3+}, Er^{3+}, Pr^{3+}, Ho^{3+}, Sm^{3+}, Tm^{3+}, Yb^{2+}, Yb^{3+}, Dy^{3+}, etc.) or transition metal ions (Cr^{3+}, Mn^{4+}, Mn^{2+}, Ni^{2+}, Co^{2+}, etc). Only a few ions (Er^{3+}, Yb^{3+}, Nd^{3+}, Pr^{3+}, Cr^{3+}, Mn^{4+}, Mn^{2+}, Ni^{2+}, Co^{2+}, etc.) have NIR emission properties. Cr^{3+}, Mn^{4+}, Mn^{2+}, RE^{3+}, Eu^{2+}, Yb^{2+}, Pr^{4+}, Ce^{4+}, Tb^{4+}, etc. play an important role in the emission in the NIR region. Yb^{2+}, Pr^{3+}, Nd^{3+}, Co^{2+}, Ni^{2+}, etc. have made great contributions to the design and synthesis of NIR-II/III LPPs.[60–68] In addition, NIR emission in the second and third regions can also be achieved through a continuous energy transfer strategy between two or more different emission centers[19,69,70] (as shown in Table 1).

3. Synthesis methods

3.1 Synthesis methods of inorganic and inorganic-organic hybrid LPPs

Synthesis methods have a significant impact on the micromorphology, afterglow properties, luminous efficiency, and defects of long afterglow materials, which are all closely related to their applications.[111] As researchers continue to explore and study their synthesis methods. Different types of synthesis methods have been discovered and reported. The high-temperature solid-state reaction method is the most ancient, mature, and widely used. The raw materials mixed by the ball mill were heated under certain temperatures and conditions.[112,113] The use of co-solvents such as P_2O_5 and B_2O_3 was discovered to lower the sintering temperature and improve the material's afterglow qualities.[114] Although the above synthesis method is simple and low-cost, it requires long-time high-temperature sintering and the prepared product is damaged by ball milling, which reduces the afterglow performance of the material. In 1990, Indian researchers used the combustion method to prepare LPPs to solve the drawbacks of the high-temperature solid phase reaction method, such as large particles and damaged crystal shape.[115] The method utilizes the heat released by the combustion reaction of the mixed raw materials to promote the spontaneous and continuous chemical reaction without a complicated heating device. In short, it is a promising synthesis method. Both Zhang[116] and Ni et al.[117] have successfully manufactured various of LPPs using this technology in recent years.

Table 1 Comparison of the afterglow properties of common NIR PLNPs and their different applications in biomedical fields

NIR partition	Different substrates	Main material	Dopant ions	Excitation	Emission	color	Afterglow time	Biomedical applications	References
NIR-I	Sulfide	CaS	Eu²⁺, Dy³⁺	254 nm	550–800 nm	Red	18 min	—	63
		ZnS	Cu, Cl/Cu, Al	Cathode ray	420–620 nm	Green	—	—	71
	Perovskite	CsPbX₃ (X = Cl, Br, I)	—	365 nm	400–700 nm	Green/red	~8 h	—	72
	Aluminate	Sr₃Al₂O₆	Eu²⁺, Dy³⁺	473 nm	550–700 nm	Red	>600 s	—	73
		LaAlO₃	Mn⁴⁺	254 nm	680–750 nm	Red	~10 min	Imaging	74
			Cr³⁺	UV	734 nm	Red	100 min	Optical imaging	76
	Gallate	SrAl₂O₄	Eu²⁺, Dy³⁺	—	~520 nm	Green	—	Imaging, monitoring	77
		ZnGa₂O₄	—	UV/LED	700 nm	Red	~2400 s	In vivo optical bioimaging and drug-delivery	78
			Cr³⁺	250 nm	695 nm	Red	~60 min	Imaging, background-free bioassay, detection of hemoglobin	79–82
				UV	700 nm	Red	>80 min	Optical imaging of vascularization, tumours and grafted cells	83
			Cr, Gd	X-ray	600–750 nm	Red	>5 min	Optical imaging	84
			Iron oxide	Red LED/UV	600–900 nm	Red	~1800 s	Multimodal imaging	85
			Cr³⁺, Bi³⁺	254 nm	650–800 nm	Red	~1200 s	Multimodal imaging	86
			Cr³⁺, Si⁴⁺	254 nm	600–700 nm	Red	~40 min	Bioenvironmental temperature sensing detection	87
		Y₃Ga₅O₁₂		655 nm	650–950 nm	Red	10 min	In vivo imaging	88
		Gd₃Ga₅O₁₂	Cr³⁺, Nd³⁺	UV	745 nm	Red	>3 h	Multimodal imaging and cancer therapy	89
		Gd₂.₉₉Ce₀.₀₁Al₁.₉₉₅Cr₀.₀₀₅Ga₃O₁₂	Cr³⁺	800 nm	650–900 nm	Red	10 min	Multimodal imaging	90
	Germanate	MgGeO₃	Mn²⁺, Yb³⁺	254 nm	300–750 nm	Red	~1800 s	—	91
		K₄CaGe₃O₉	Mn²⁺, Yb³⁺	254 nm	300–700 nm	—	5 h	—	92
	Gallium germanate	Zn₁.₁Ga₁.₈Ge₀.₁O₄	Cr³⁺	UV	690–750 nm	Red	10 min	Bioenvironmental testing	93
				LED, Red LED	695 nm	Red	1 h, 2 h	Drug delivery, chemotherapy	95
		Zn₁.₁Ga₁.₈Ge₀.₁O₄	Cr³⁺, Eu³⁺	696 nm	700–800 nm	Red	50 min	Drug delivery and tumor targeted imaging	96
				254 nm	675–750 nm	Red	3 h	In vivo chemotherapy	97
		Zn₁.₂₅Ga₁.₅Ge₀.₂₅O₄	Cr³⁺, Yb³⁺, Er³⁺	254 nm	660–780 nm	Red	50 min	Drug delivery	98
	Titanate	CaZnTiO₃	Pr³⁺	314 nm	600–650 nm	Red	>2.5 h	Photothermal therapy, biomonitoring	99
		Na₀.₅Gd₀.₅TiO₃	Cr³⁺	650 nm	760 nm	Red	~60 min	Low-irradiance imaging	100
	Nitride	Ba[Mg₂Al₂N₄]	Eu²⁺, Tm³⁺	660 nm	600–900 nm	Red	~1000 s	—	18
	Stannate	SrSnO₃	Bi²⁺	808 nm	700–900 nm	Red	>30 min	In vivo bioimaging	101
		Sr₂SnO₄	Tm³⁺	254 nm	440–850 nm	Red	>30 min	—	64
	Other	F-L-Yb	—	980 nm	900–1100 nm	Red	500 µs	Time-resolved imaging	102
		Conjugated polymers MEH-PPV	—	465 nm	780 nm	Red	~1 h	Tracking and molecular optics imaging	103
		Semiconductor polymers SPNs	—	Biothio-activation	780 nm	Red	~30 min	Detection of drug-induced hepatotoxicity	104
		Luminous nanodots AGL AIE dots	—	465 nm	600–650 nm	Red	250 s	Surgical imaging navigation	105
		Bioluminescent probes FD-1029	—	560 nm	1029 nm	Red	300 min	NIR-II imaging	106
		Nanocomposites LPLNP-PPT/TRAIL	—	254 nm	694 nm	Red	~2 h	Mesenchymal stem cell therapy engineering (MSC) treatment and follow-up	107

Table 1 (Contd.)

NIR partition	Different substrates	Main material	Dopant ions	Excitation	Emission	Emission color	Afterglow time	Biomedical applications	References
NIR-II/III	Fluoride	$NaYF_4/NaGdF_4/NaLuF_4$	Ln^{3+}/Tb^{2+}	X-ray	480–1060 nm	Green/red	>1800 s	Bioimaging	13–15
	Titanate	$CaTiO_3$	Yb^{3+}, Bi^{3+}	365 nm	900–1100 nm	Red	>80 h	—	67
	Gallium germanate	$Zn_3Ga_2Ge_2O_{10}$	Ni^{2+}	300 nm	900–1700 nm	Red	>2 h	—	65
	Stannate	$Zn_2Ga_2Sn_{0.5}O_6$	Yb^{3+}, Ni^{2+}	254 nm	1100–1600 nm	Red	>5 min	—	66
	Gallate	$Y_3Al_2Ga_3O_{12}$	Cr^{3+}, Er^{3+}	254 nm	690 nm, 1532 nm	Red	~1000 min	—	19
			Nd^{3+}, Ce^{3+}, Cr^{3+}	460 nm	850–1200 nm	Red	>10 h	—	69
		$ZnGa_2O_4$	Co^{2+}, Ni^{2+}	—	900–1700 nm	Red	>30 min	—	68
		$Zn_{1+y}Sn_yGa_{2-x-2y}O_4$	Ni^{2+}	UV	1270–1430 nm	Red	~300 s	With potential for optical imaging	108
	Aluminates	$Zn_{0.6}Ca_{0.4}Ga_2O_4$	Cr^{3+}, Yb^{3+}	254 nm	950–1100 nm	Red	>10 min	With potential for optical imaging	109
		$LaAlO_3$	Cr^{3+}/Er^{3+}	UV	734 nm, 1553 nm	Red	~60 min	With potential for optical imaging in vivo	60
	Phosphate	$Ba_3(PO_4)_2$	Mn^{5+}	200–900 nm	1100–1300 nm	Red	550 s	In vivo NIR-II fluorescence imaging	110

During the synthesis of various LPPs, it was discovered that the afterglow properties and particle shape of the materials can be greatly improved by doping with different types and contents of rare earth or transition metals, or even by adding alcohol and other substances in the synthesis.[118,119] However, the existing traditional synthesis methods have been unable to meet the requirements of high-doping content or controlled appearance of materials. Gradually, the sol-gel method, co-precipitation method, and template method were developed. These methods have proven to be effective in improving LPPs with desirable properties. Nevertheless, a drawback that should not be overlooked is that these methods do not provide direct access to LPPs and require a traditional calcination process. The advent of hydrothermal synthesis has made sudden progress in the field of preparation, which not only greatly reduces the temperature of the reaction, but also enables the synthesis of products in a single step. In recent years, Yang,[120] Ankoji,[121] Wang,[122] and other teams have successfully prepared different LPPs with excellent afterglow properties using this method using high-temperature and high-pressure reactors. The synthesis conditions in this method are mild, and the particles are nanoscale and uniform. Of course, there are also disadvantages such as being limited to the oxidation system and reducing the brightness of the product. With the rapid development of modern science and technology, the synthesis methods of LPPs are also advancing, and many new methods are emerging, such as microwave method,[123] flame spray pyrolysis,[124,125] vapor deposition,[126,127] electrostatic spinning,[128,129] and ultrasonic synthesis.[130,131] Fig. 5 shows a brief flowchart of the different synthesis methods. In short, researchers are making progress toward better LPP synthesis. A comparison of different common synthesis methods of LPP in terms of preparation time, temperature, and morphological appearance is shown in Table 2.

3.2 Design strategies for organic LPPs

Thus far, crystal induction,[145] hydrogen bonding effect,[146,147] host–guest doping,[148] and other methods have been used to create a rigid environment, which effectively reduces the non-radiative leap rate. The high nuclear charge of halogen atoms with heavy atomic effect[149,150] effectively enhances the inter-system scramble of molecules in the S_1 state to form a stable triple excited state, resulting in the organic long afterglow phenomenon. The difficulty in obtaining pure organic LPPs can be attributed to two major factors. Firstly, the spin coupling between the lowest excited singlet state (S_1) and the lowest excited triplet state (T_1) is very weak in pure organic material molecules. The second reason is that the non-radiative leap rate is fast enough to allow the absorbed energy to be radiated as heat or other forms of energy.[151] Therefore, researchers have focussed on developing organic LPPs with an excellent performance by increasing the probability of intersystem crossing, stabilizing triplet excited states, or reducing nonradiative transition rates. From both molecular and material design perspectives, organic ultra-long phosphorescence emission at room temperature has been achieved in a series of material
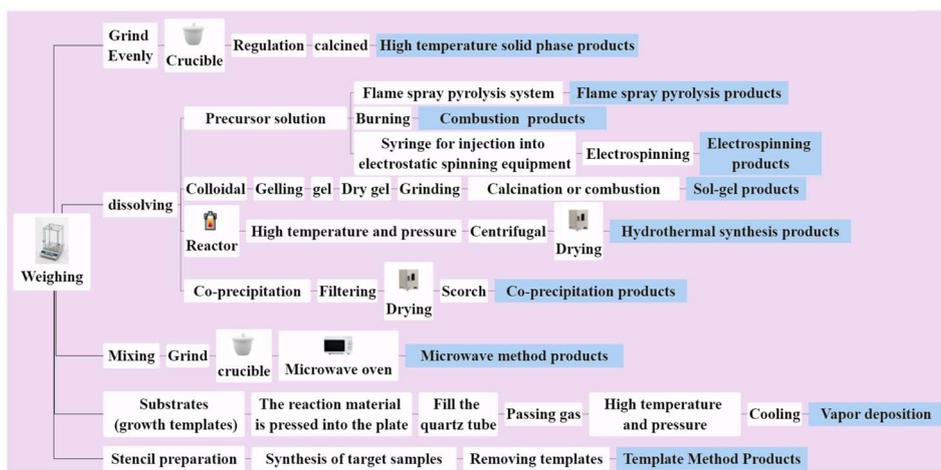
Fig. 5   Several brief flow charts for the preparation of LPPs.

systems, including single-component crystals, multi-component crystals, carbon dots, and polymers.

In terms of molecules, organic LPPs can be created by incorporating aromatic carbonyl groups, heavy atoms, heavy atoms, heteroatoms containing lone pairs of electrons and paramagnetic molecular groups,[152–155] deuterium substitution,[156] host–guest doping,[157,158] aggregation structures,[159,160] etc. for materials; they can be designed by rigid structure induction,[161–163] polymer formation,[164] resonance structures,[165] and thermal activation.[166] Most reported materials have been carefully designed and synthesized. Organic LPPs urgently should start from the existing afterglow materials and design the construction strategy of organic LPPs without any chemical modification. Table 3 shows the design strategies for organic LPPs.

4.   NIR LPPs in biomedical applications

In biological applications, NIR LPPs can avoid auto-fluorescence of biological tissues without situ excitation, while they have excellent afterglow properties in the NIR region. NIR LPPs exhibit superior responsiveness and biological tissue penetration compared to standard LPPs, boosting detection signal-to-noise ratio and sensitivity while minimizing background noise.[11] The afterglow properties of NIR LPPs are changeable under different substrates or even the same substrate under varied doping conditions, allowing for a wide range of applications. As shown in Table 1, we compared the afterglow properties and biomedical applications of different NIR LPPs. NIR LPPs commonly used in the biomedical field are nanoscale, which are called NIR-persistent luminescence nanoparticles (PLNPs). Thanks to ongoing research and functionalized modifications by researchers, NIR PLNPs have been used in a variety of fields, including biosensing detection, bioimaging, drug delivery, and cancer therapy.

4.1   Biosensing detection

NIR PLNPs can be used as bioprobes for monitoring and identifying changes in the biological environment in the field of sensing and monitoring biomarkers. Currently, researchers have developed a number of biological probes based on NIR PLNPs for monitoring various active chemicals in living organisms. These probes have high sensitivity, signal-to-noise ratio, and excellent detection performance.

4.1.1   Detection of proteins.
In 2012, Maldiney et al. used biotin-coated Eu, Dy, and Mn-doped silicate nanoparticles to detect avidin for the first time.[167] It is a pioneer in protein detection using materials. At present, it has been used to detect various proteins such as hemoglobin (Hb), alpha-fetoprotein (AFP), and others.[82,168] Hb plays a crucial role in the transport of oxygen atoms in mammals. It is also a typical biomarker for certain diseases, such as leukemia, heart disease, and anemia.[169,170] Although many detection techniques have been developed, the detection of Hb in red blood cells still suffers from low sensitivity and poor specificity. Liu et al.[82] synthesized a $ZnGa_2O_4$:Cr (ZGC) probe with water-soluble and NIR luminescence properties. It was found that Hb could neither shield the probe's excitation light nor absorb its emission, but could rapidly quench it. There is a partial overlap between the absorption spectrum of Hb and the emission spectrum of the probe, which is different from the common energy transfer mechanism. Therefore, it is classified as a typical collisional quenching process. The dynamic quenching mechanism gradually and significantly suppressed the persistent luminescence phenomenon with the addition of hemoglobin. The probe has a specific response to hemoglobin, laying the groundwork for hemoglobin detection. Fig. 6a shows a diagram of this probe for the ultra-sensitive detection of hemoglobin. It also possesses great selectivity and ultra-sensitivity to Hb due to its easy operation, and this technology has been effectively used in the clinical detection of human Hb content.

Serum levels of AFP can rise abnormally in conditions such as chronic hepatitis, cirrhosis, and liver cancer. The current clinical serum marker to determine primary liver cancer is

Table 2 Comparison of common preparation methods for LPPs in various aspects

Preparation method	Preparation principle	Preparation time	Preparation temperature	Advantages	Disadvantages	Grain size	Ref.
High temperature solid state reaction method	Combustion between solid powders	A few hours	>1000 °C	Simple process, convenient operation, low cost, high brightness, wide range of applications	High temperature, long time, large particles	Micron level	74
Combustion method	High temperature scorching	A few minutes	>1000 °C	Shorter time and more energy efficient than high temperature solid phase reaction preparation	A large amount of ammonia gas will be generated and pollute the environment. Lower brightness than the product synthesized by high temperature solid phase reaction method	Nanoscale to micron scale	133
Sol–gel method	Sol–gel pathway and polymerizable complex pathway	A few hours	≤200 °C	Good product uniformity, small particle size, strong luminosity	An auxiliary method. High cost and long duration. More damaging to the organism	Nanoscale to micron scale	135–138
Hydrothermal synthesis method	Closed environment high temperature and high pressure synthesis	A few hours	100–240 °C	Mild synthesis conditions, stable system, uniform particle	Low brightness, limited to oxide system	Nanoscale to micron scale	139–141
Co-precipitation method	Sedimentation principle	A few hours	Room temperature	Smaller particle size, higher purity, more uniform particles, and longer process compared to high-temperature solid phase reaction products	An auxiliary method. Easy to generate other impurity mixture, temperature is not easy to control	Nanoscale to micron scale	142
Template method	Use of extrinsic templates to control material appearance	A few hours	Room temperature	Uniform particle size, easily controlled size and shape, mild conditions	An auxiliary method. The stencil is more restrictive on the morphological pattern	Nanoscale to micron scale	109
Vapor deposition	Chemical or physical changes occur between gases and coalesce after cooling	A few minutes	>1000 °C	No polluting gas is released during the reaction, and the product is bright, which is a clean and energy-saving preparation method	High cost	Nanoscale to micron scale	126
Microwave method	Heating with microwave	A few hours	—	Fast and efficient, energy-saving, simple operation, uniform particles, less pollution	Not well suited for industrial production	Nanoscale to micron scale	123
Flame spray pyrolysis	Using surface tension, electric field force, coulomb force, and other interactions	Depending on the flow rate of oxygen in the generator, generally 5 L min^{-1}	>1000 °C	Fast and efficient, uniform particles, low strength, no pollution	High cost and long time	Micron level	124
Electrostatic spinning	Use of polymer electrostatic atomization form	Depending on the speed of the electronic pump injection, generally 2 ml h^{-1}	>1000 °C	Uniform size, easy to control shape and appearance, high brightness, simple and easy to operate	High cost, easy to cause environmental pollution	Nanoscale to micron scale	128

Table 3 Design strategies for organic LPPs

Type	Design strategy	Reason	Applications	Ref.
Molecular design	Introduction of aromatic carbonyl groups, heavy atoms, heteroatoms containing lone pairs of electrons, and molecular groups with paramagnetic properties	Promote $n–\pi^*$ jumps, enhance inter-system scramble processes, and increase the stability of triple excited states	Application to small molecule crystals, organic ionic crystals, carbon dots, and other single-component series	152–155
	Deuterated	Weakening the intramolecular vibrations and reducing the rate constant of the non-radiative decay of the triple excited state	Organic molecules have a large number of hydrogen atoms present, and under certain conditions, they can all be deuterated	156
Material design	The role between the subject and object molecules	Restriction of guest molecular motion and inhibition of non-radiative leaps	Application to multi-component eutectic, host–guest doping, amorphous films, and other types	157
	Construction of effective aggregation structures (e.g. H aggregation structures, strong $\pi–\pi$ stacking, ionic bonding, etc.)	Inhibition of nonradiative leaps, stabilization of trilinear excitons, and slow release	Application to organic ionomers, materials containing π-bonds, etc. that are prone to forming aggregate structures	159
	Rigid solid-phase crystalline structure induced	Introduction of amine groups, carboxyl groups, carbonyl groups, etc. groups, carbonyl groups, etc., to improve molecular interactions	Application to single crystal and eutectic systems	161–163
	Formation of polymers	Stabilization of the triplet state in organic molecules to reduce the non-radiative deactivation of the triplet state (T_1) to the ground state (S_0)	For example, single component room temperature phosphorescent polymers in solid films or nanoparticles	164
	Resonant structures	More inter-system crossing channels, significantly enhanced the self-selected orbital coupling effect, facilitating the inter-system crossing	Afterglow molecules based on the existence of resonance structures such as $N–P=O/N–P=S$	165
	Thermal activation process	A special type of three-mode emission that can be produced by the radiative decay of S_1, T_1, and T_1^* at room temperature	In distorted donor–acceptor structure afterglow molecules	166

AFP. Therefore, the measurement of serum AFP levels can be used as a diagnostic criterion for early liver disease.[171,172] In 2011, an assay for the inhibition of AFP by fluorescence resonance energy transfer (FRET) was reported by Yan et al.[168] They used polyethyleneimine (PEI) for the surface functionalization of $Ca_{1.86}Mg_{0.14}ZnSi_2O_7$:$Eu^{2+}$, Dy^{3+} water-soluble PLNPs were first synthesized. At this time, the material will have a long afterglow in the NIR after being excited by the UV. After coating with gold nanomaterials, the long afterglow phenomenon will disappear. This work exploits the fact that AFP can disrupt the structure of PEI PLNPs and restore their afterglow properties to detect AFP in serum. A schematic diagram of the PLNPs for the determination of AFP content is shown in Fig. 6b. The detection method has also been successfully applied to the clinical detection of AFP content in human serum, which is of great significance for the early detection of liver cancer.

4.1.2 Detection of the biological environment. NIR LPPs can be used not only for tracking and monitoring biological environments in vitro but in vivo. For example, tracking macrophages and visualizing inflammatory tissue. Significantly, NIR LPPs are functionally modified and typically coated with polyethylene glycols, folic acid, and other compounds prior to bioavailability to improve drug delivery and biosafety. It has been found that the NIR LPPs modified by surface functionalization can achieve low or even non-toxic effects, which is a very
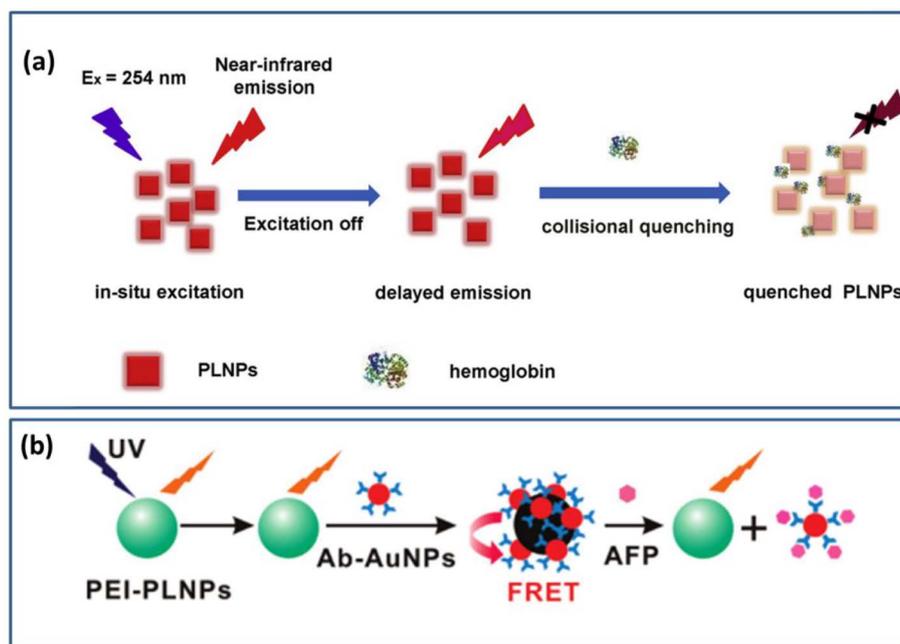
Fig. 6 (a) Schematic diagram for ultra-sensitive detection of hemoglobin. Reproduced from ref. 82 with permission from Elsevier, copyright 2020. (b) Schematic diagram of these PLNPs for the determination of AFP content. Reproduced from ref. 168 with permission from the American Chemical Society, copyright 2011.
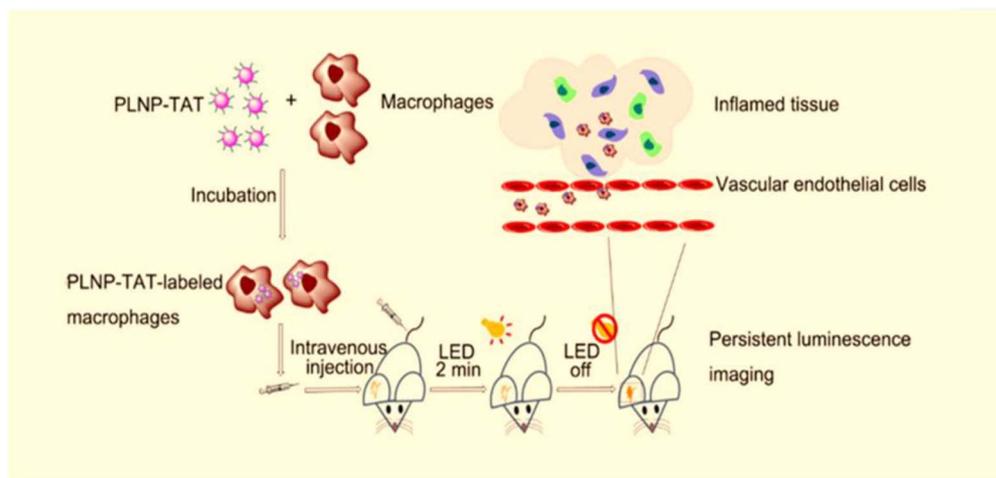

Fig. 7 Schematic representation of PLNP-TAT labeled macrophages homing to inflammatory tissues. Reproduced from ref. 93 with permission from the American Chemical Society, copyright 2019.

ideal material for biological probes.[83,173] Sun et al.[174] used a sol-gel method to create $Zn_{1.1}Ga_{1.8}Ge_{0.1}O_4{:}Cr^{3+}$ (ZGG) with low cytotoxicity and NIR-sustained luminescence properties, which they used to create a model for tracking the inflammatory tissue in mice in 2018. This study demonstrated a simple and novel method for visualizing inflammation *in vivo* with high sensitivity, paving the way for a new method for the early detection of 12 inflammation-related diseases. The following year, Chen et al.[93] reported cell-penetrating peptide-functionalized LPPs (PLNP-TAT) as a luminescent marker for non-invasive tracking of J774A.1 macrophages in a mouse model of inflammation.

Fig. 7 shows a schematic diagram of PLNP-TAT-labeled macrophages homing to inflamed tissues.

In addition, it is also useful in the construction of surgical guidance systems. Tissue autofluorescence can be efficiently prevented because ZGGO:Cr particles can sustain NIR luminescence after stimulation stops. Wang et al.[94] demonstrated that the ZGGO:Cr particles created are suitable candidates for autofluorescence-free bioimaging. By building an aptamer-guided ZGGO:Cr bioprobe, it can be used for real-time monitoring of biological processes and the development of surgical guidance systems.

4.2 Bioimaging

The excellent chemical stability and photostability of NIR LPPs lay the foundation for their application in biomedicine. Bio-imaging takes advantage of the continuous luminescence of the material after excitation with different wavelengths of light, such as X-rays, UV, and LED lights.[15,84,93–95] Regarding biological imaging, various different techniques have been developed, such as optical imaging, up-conversion imaging, magnetic resonance imaging, time-resolved imaging, and other single-modality imaging techniques and multi-modality imaging techniques.

4.2.1 Optical imaging. Optical imaging technology is a type of imaging that converts optical signals into electrical signals by exploiting the unique optical differences between the area to be imaged and the background (such as light scattering, absorption, luminescence, *etc.*).[175] This technique not only allows for *in vitro* diagnosis, such as cellular or single-molecule diagnostics, but it also allows for image guidance during surgery, such as tumor excision and minimally invasive surgery *in vivo*. Utilizing

BALB/carbon nude mouse molds, Lin *et al.*[84] generated PLNPs [SiO$_2$@ZnGa$_2$O$_4$:Cr^{3+}@SiO$_2$ (SZGOS)] using a simple silica template approach for *in vivo* NIR luminescence imaging. Model mice injected intravenously with a certain dose of SZGOS solution were found to have a high concentration of luminescent material in the liver area after a period of irradiation with soft X-rays. This phenomenon was used as a target area for the effect of SZGOS luminescence imaging *in vivo*. The main signal of persistent luminescence was detected in the liver region for more than 2 hours by observing the persistent luminescence images (Fig. 8a). Notably, upon re-irradiation with soft X-rays, the luminescence signal was fully activated again, indicating that the nanomaterial can be repeatedly activated in situ for long-term imaging *in vivo* (Fig. 8b). In the same year, Katayama *et al.*[76] also developed LaAlO$_3$:Cr^{3+}, which can continuously emit light at 734 nm in the NIR-I after being activated by Cr^{3+}. By observing the phenomenon of light transfer and the induced continuous emission, it is proved that this material can be used for repeated imaging *in vivo*.
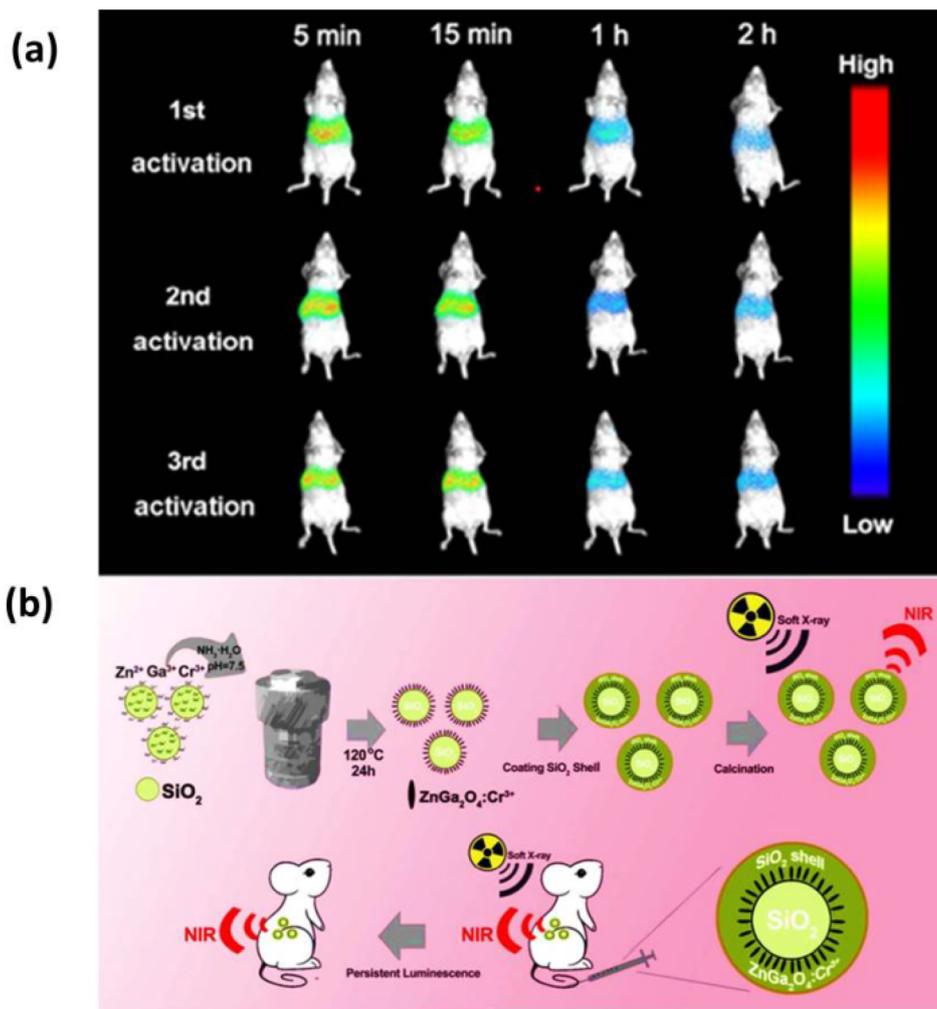

Fig. 8 (a) Continuous luminescence imaging of soft X-ray activated BALB/carbon nude mice by intravenous injection of SZGOS solution. (b) Schematic diagram for the synthesis of SZGOS nanoparticles and their application in long-term *in vivo* bioimaging. Reproduced from ref. 84 with permission from the American Chemical Society, copyright 2017.

4.2.2 Fluorescence lifetime imaging. Fluorescence lifetime imaging (FLIM) is the best *in vivo* time-resolved imaging technique available. Not only does it penetrate deep into the tissues in the NIR region of 650–1800 nm, but it also offers the unique advantage of quantitative visualization of molecular events *in vivo*. It is also independent of local luminescence intensity, fluorophore concentration, and biological tissue thickness. It is well known that the fluorescence lifetime and afterglow mechanisms are different. The fluorescence lifetime refers to the time for an electron to transition from the excited state back to the ground state. In contrast, afterglow refers to the process of capturing and releasing electrons. Due to the long lifetime of lanthanides, Ning *et al.*[102] designed and synthesized a sensitive Yb^{3+} probe with deep permeability, good reversibility, and high spatial and temporal resolution, which is capable of in situ real-time dynamic monitoring pH changes, *in vitro* and *in vivo* (Fig. 9a shows the synthesis schematic for the design of a Yb^{3+} probe). The advantages of NIR emitting Ln for molecular imaging *in vivo* were also successfully demonstrated in a mouse model for monitoring pH in the gastrointestinal tract *in vivo*, as shown in Fig. 9b and c for the fluorescence imaging intensity and FLIM imaging.

4.2.3 Nuclear magnetic resonance imaging. Based on different attenuation for the energy released in different structural environments within a substance, magnetic resonance imaging (MRI) is the imaging of electromagnetic waves emitted through the detection of an applied gradient magnetic field using the principle of nuclear magnetic resonance. This imaging technique is a promising technical imaging tool, which is multi-parametric and high-contrast imaging without damage.[176,177] Wang *et al.*[178] used hydrothermal synthesis to create NIR PLNPs ($ZnGa_2O_4$:Cr^{3+}) and used these PLNPs to create a multimodal probe from hyaluronic acid functionalized Gd_2O_3 (HA-Gd_2O_3). As shown in Fig. 10a, the preparation of HA-Gd_2O_3-PLNPs probes is shown schematically. HA-Gd_2O_3 was used as an MRI contrast agent and PLNPs as a light source. *In vivo* imaging was successfully achieved in mice under the excitation of LED. The potential of multimodal probes for tumor-targeted NIR sustained luminescence and magnetic resonance imaging *In vivo* and *in vitro* was demonstrated.

Wang and Li *et al.*[179] synthesized PLNPs using mesoporous silica nanoparticles (MSNs) as a template. After excitation with 254 nm light for 15 min, it could exhibit long afterglow properties in the NIR range of 750–800 nm. Magnetic resonance dual-mode imaging was achieved by fine-tuning the
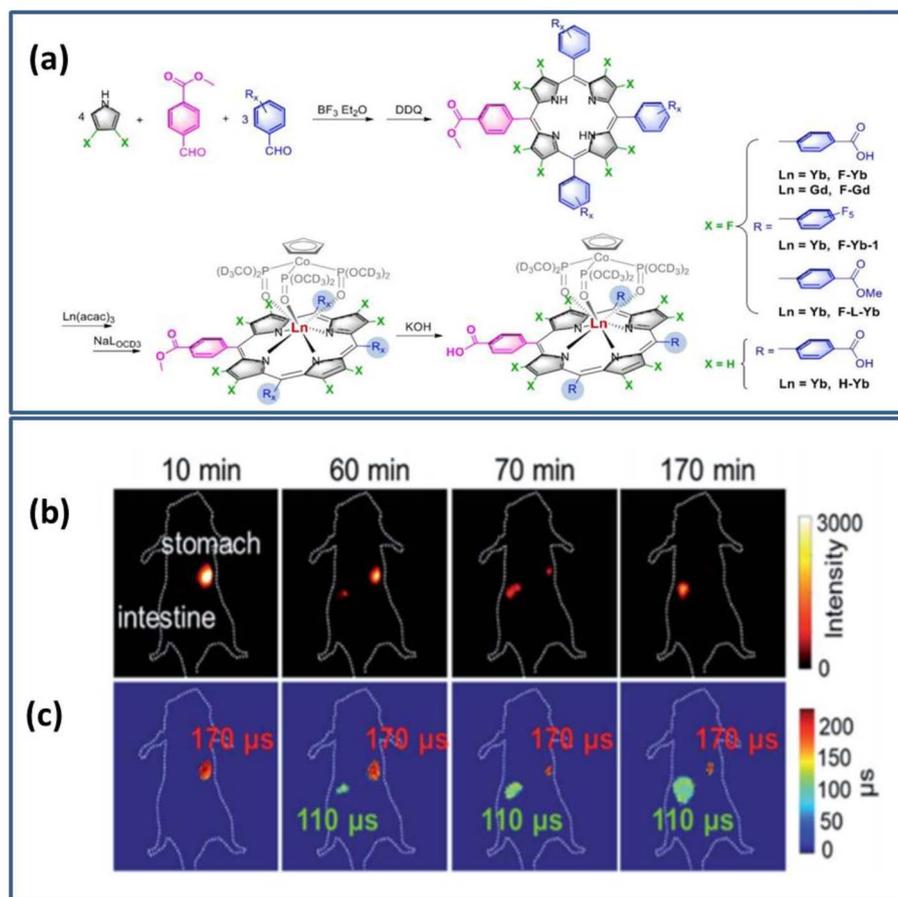

Fig. 9 (a) Schematic diagram of the design and synthesis of the Yb^{3+} probe (b) NIR intensity fluorescence imaging (exposure time, 25 ms) (c) FLIM image (exposure time, 250 ms). λ_{ex} = 532 nm; λ_{em} = 1000 nm long range. Reproduced from ref. 102 with permission from the Royal Society of Chemistry, copyright 2019.
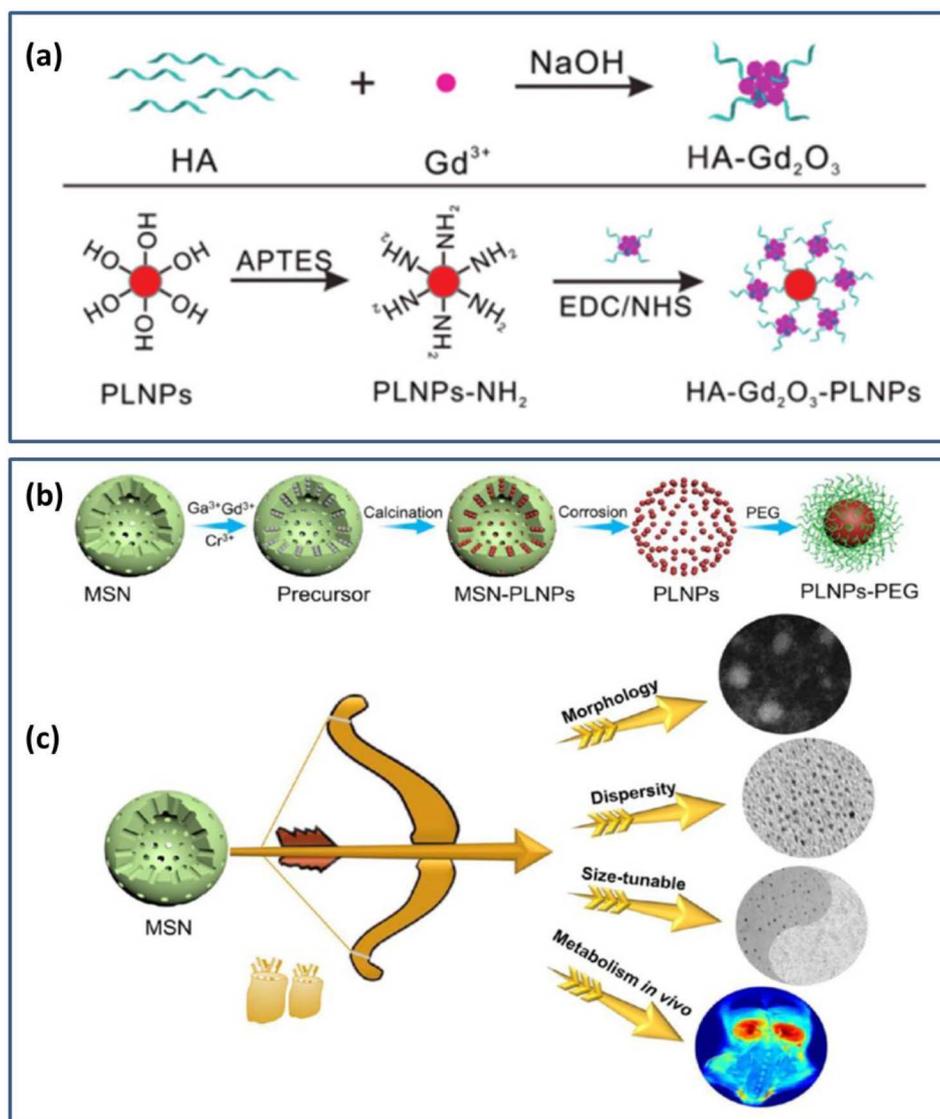
Fig. 10 (a) Schematic diagram for the preparation of the HA-Gd$_2$O$_3$-PLNPs probe. Reproduced from ref. 178 with permission from the Royal Society of Chemistry, copyright 2017. (b) Synthesis and surface functionalization of MSNs. (c) Performance optimization of MSNs. Reproduced from ref. 179 with permission from the American Chemical Society, copyright 2021.

morphology, size dispersion, and other properties of this material after coating it with polyethylene glycol. Fig. 10b and c are schematic diagrams of the synthesis and modification of the material, as well as the fine-tuning of the material properties. More notably, this work achieved renal clearance without toxicity to the organism, further promoting the application of the material in kidney-related diseases and cancer.

4.2.4 Multimodal imaging. In addition to unimodal imaging applications, multimodal imaging techniques integrate two or more imaging modalities and can be used to diagnose diseases, mediate surgery, and so forth. Multimodal imaging can overcome the limitations of unimodal techniques and take advantage of each unimodal imaging technique to observe lesions with higher specificity, which provides a more powerful technical tool for treating diseases and curing the untreated. Abdukayum et al.[180] achieved the first combination of

NIR optical imaging and MRI by coupling gadolinium spray glucosamine (Gd-DTPA) with PLNPs. Sengar et al.[90] firstly used a synthetic Gd$_{2.99}$Ce$_{0.01}$Al$_{1.995}$Cr$_{0.005}$Ga$_3$O$_{12}$ (GAGG:Ce, Cr) multimode probe for host cell imaging and cytotoxicity experiments. After the surface functional modification of folic acid, the probe has the potential of two-photon bioimaging in the NIR I region (650–900 nm) under the excitation of two-photon NIR (800 nm). In addition, the material has good paramagnetic properties, so it can be used for MRI. The researchers also performed toxicity tests on four different cell lines, demonstrating that the probe has not only good biocompatibility but also low toxicity, which achieved two-photon excitation imaging and NMR imaging. The following year, the group of Maldiney combined superparamagnetic iron oxide nanoparticles with chromium-doped zinc gallate, which was the first bimodal optical MRI nanoprobes (MPNHs) based on the

development of magnetic persistent nanoparticles obtained from red light technology. The probe not only realizes real-time imaging with high spatial resolution *in vivo* but also laid the foundation for magnetic vectorization and cell therapy *in vitro*.[86] Simultaneously, they attempted to use Gd ions instead of iron oxide nanoparticles to combine with chromium-doped zinc gallate. They also built a probe of the same type, which successfully realized real-time monitoring and imaging after the surface functional of polyethylene glycol. Under the surface functional modification of polyethylene glycol, the probe can significantly delay the uptake of the reticuloendothelial system *in vivo* when injected into healthy mice, providing novel nano-technology for diagnosis in the biomedical field.[85]

In recent years, researchers have investigated and studied NIR LPPs after they have entered the human body through various routes. The goal is to improve imaging targeting and develop better administration routes, indicating their bright future for *in vivo* bioimaging. In 2016, Li *et al.*[141] compared the targeted of synthetic monodisperse tridoped zinc gallate (ZGGO:Cr^{3+}, Yb^{3+}, Er^{3+}) after surface functionalization with folic acid by using both gavage and caudal intravenous routes of administration. Fig. 11 shows the fabrication of the material, surface functionalization modification, and oral *in vivo* imaging, schematically. The targeting performance of orally folic acid functionalized ZGGO:Cr^{3+}, Yb^{3+}, Er^{3+} for tumor-targeted bioimaging is shown to be superior to that of traditional intravenous injection for the first time, indicating a good strategy for disease detection and drug delivery route selection.

4.2.5 NIR-II/III bioimaging. The longer the wavelength, the greater the penetration of biological tissue and the lesser the corresponding damage. The second and third regions of NIR light are gaining popularity. Shi *et al.*[89] constructed a multifunctional nanoplatform from Cr^{3+}, Nd^{3+} co-doped $Gd_3Ga_5O_{12}$ synthesized using the template method, which exhibited excellent luminescence performance at 1067 nm under excitation at 808 nm. These particles also have a magnetic resonance effect due to the presence of Gd. Coupled with NIR-II luminescence properties, it exhibited multimodal imaging properties. Nie *et al.*[108] successfully prepared Ni^{2+}-doped $Zn_{1+y}Sn_yGa_{2-x-2y}O_4$ nanomaterials. The emission peaks in the second emission window in the NIR range from 1270 to 1430 nm. During the tunability, high resolution and low light interference could be achieved, it provides greater application potential in the biomedical field. Er^{3+}, Cr^{3+}, and Sm^{3+}-doped $LaAlO_3$ nanomaterials reported by Xu *et al.*[60] are promising biological probes with NIR-I (734 nm) and NIR-II (1553 nm) luminescence properties. *In vivo* optical imaging, especially in the NIR-III biological window, has great application potential.

4.3 Cancer treatment

There is currently no cure for cancer; it is one of the deadliest diseases in the world today. It is a new biomedical technology that organically combines diagnosis, monitoring, and treatment of the disease.[181,182] LPPs have made significant contributions to the field of cancer diagnosis and treatment through their unique persistent luminescence properties. Researchers have combined drugs with LPPs to guide adjuvant-targeted cancer therapy and surgical guidance through persistent luminescence imaging.[89,183] Up to now, there are different treatments such as drug delivery, chemotherapy, photothermal therapy, and photodynamic therapy.
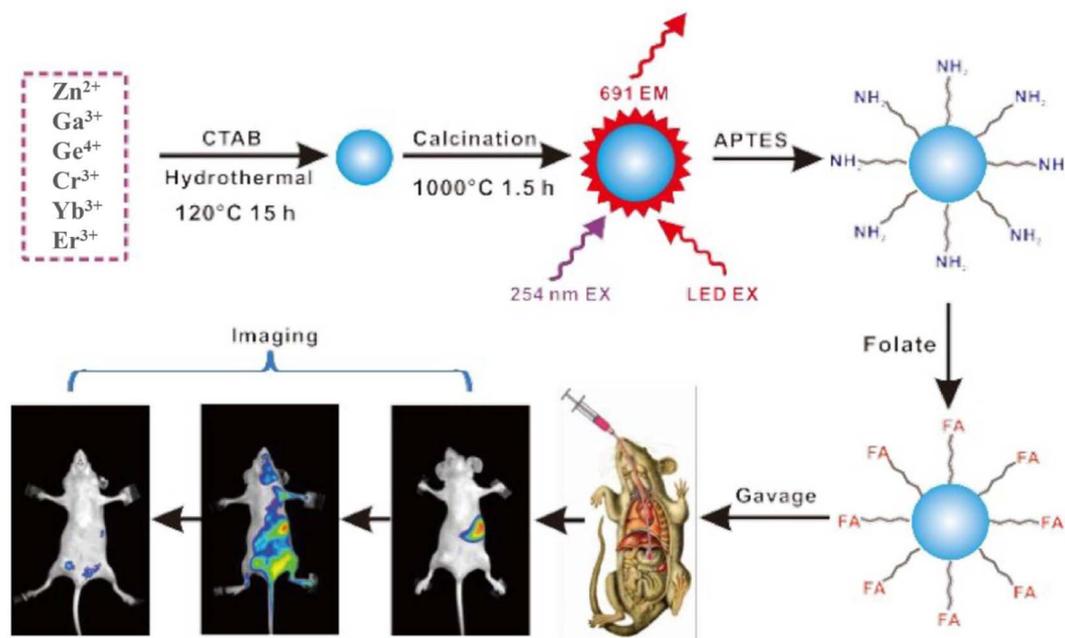

Fig. 11 ZGGO:Cr^{3+}, Yb^{3+}, Er^{3+} synthesis and surface functionalization for oral *in vivo* bioimaging. Reproduced from ref. 141 with permission from the Royal Society of Chemistry, copyright 2016.

4.3.1 Drug delivery. Drug carrier refers to control of the distribution in the organism and the release rate of the drug by changing the route of administration, so as to deliver the drug to the target tissue or organ. It can deliver some defective drugs with high side effects or poor solubility into the body, thereby reducing damage to the human body and improving drug efficacy.[184] For example, mesoporous silica and liposomes are commonly used drug-coating materials. In 2014, Maldiney et al.[78] successfully constructed a core–shell structure optical imaging probe using mesoporous silica and chromium-doped zinc gallate, which was particularly used for the optical detection of living tissue and drug delivery. The probe successfully loaded the anticancer drug doxorubicin, which started the gradual release of the disease in a pH-sensing manner, showing the advantages of drug release localization and non-invasiveness.

In addition to conventional drugs as carriers in vitro, biofilm-camouflaged drug carriers usually have better biocompatibility. Liu et al.[98] combined RBC membrane vesicles and PLNPs (ZGGO@mSiO$_2$) into RBC bio-nanoprobes using bionanotechnology. Due to the long afterglow features of PLNPs in the NIR, adriamycin was employed on this probe, which can be used for long-term bioimaging and monitoring of mice in situ. This study demonstrates that medications are successfully transported to the tumor's growth site, resulting in tumor growth reduction. Various nanoplatforms for the application of bionanotechnology to the diagnosis and treatment of diseases have been proposed. Fig. 12 shows the preparation of erythrocyte membrane bio-inspired PLNP nanocarriers for imaging and drug delivery in vivo.

4.3.2 Chemotherapy. Chemotherapy is currently the most commonly used cancer treatment in clinical practice. Although it has obvious therapeutic effects, it has disadvantages such as poor targeting, relatively large side effects, and large damage to normal cells of the human body.[181] With good biocompatibility, biodegradability, and low toxicity, liposomes are a classical and widely used carrier, which can be well used for drug delivery and cancer therapy when intelligently combined with rare earth-

doped NIR LPPs. In 2019, Zhang et al.[97] used a hydrothermal synthesis method combined with further calcination to create a hydroxylated probe ($Zn_{1.1}Ga_{1.8}Ge_{0.1}O_4$:0.5%$Cr^{3+}$, 0.5%$Eu^{3+}$). The design synthesis strategy is depicted schematically in Fig. 13a. HepG2 tumor-bearing mice were subjected to in vivo chemotherapy after surface functional modification and drug-loading system (PHLIP-SS-GFLG-MSPLNPs). Fig. 13b is a schematic diagram of continuous tumor luminescence imaging and chemotherapy.

4.3.3 Photothermal therapy. Photothermal therapy (PTT) is a treatment method for killing cancer cells by injecting materials with high photothermal conversion efficiency into the human body and then converting light energy into heat energy to gather around tumor tissues through targeted identification technology under the irradiation of external light sources. Despite growing interest, the method is still in its early stages and faces numerous challenges. Indocyanine green (ICG) for PTT guidance has great potential in cancer therapy. Zheng et al.[99] first designed and prepared ICG and LPPs co-loaded mesoporous SiO_2 nanocarriers [(ICG+PLPs)@mSiO$_2$], which were successfully used for persistent luminescence imaging-guided PTT (Fig. 14). Chen et al.[185] also developed a multi-chargeable mesoporous SiO_2/$ZnGa_2O_4$:Cr^{3+}(mZGC) NIR LPPs, which was successfully applied to photoluminescence imaging-guided PTT by loading ICG into ICG@mZGC.

4.3.4 Photodynamic therapy. Photodynamic therapy (PDT), a newly emerged clinical cancer treatment method using photosensitizers, involves irradiating the tumor site with specific wavelengths to selectively activate the photosensitized drugs gathered in the tumor tissue to produce singlet oxygen (ROS) thereby killing cancer cells. This method requires long-time irradiation of visible light or ultraviolet light, which not only limits tissue penetration and penetration strength but also causes skin and tissue damage. However, the afterglow characteristics of NIR long-persistence luminescent materials can be used as the internal persistent light source of PDT, which can allow deep tissue treatment and avoid skin tissue damage.[186,187] Fan et al.[188] successfully constructed an injectable ZGC-
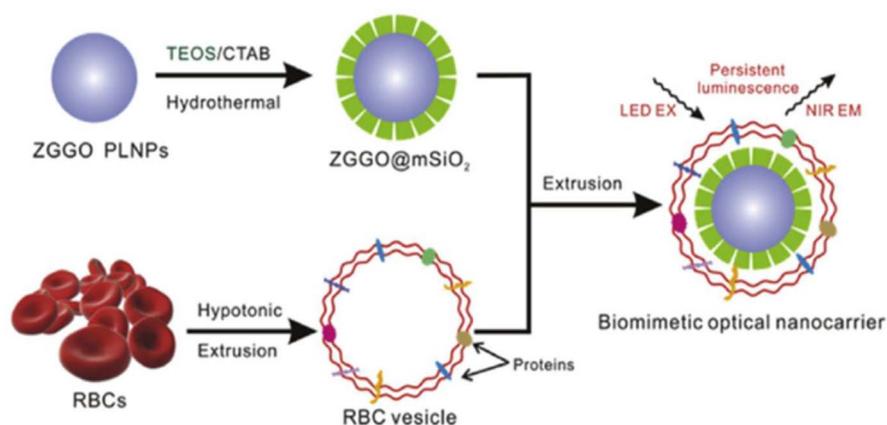

Fig. 12 Schematic diagram of the preparation of erythrocyte membrane bioinspired PLNP nanocarriers for imaging and drug delivery in vivo. Reproduced from ref. 98 with permission from Elsevier, copyright 2018.
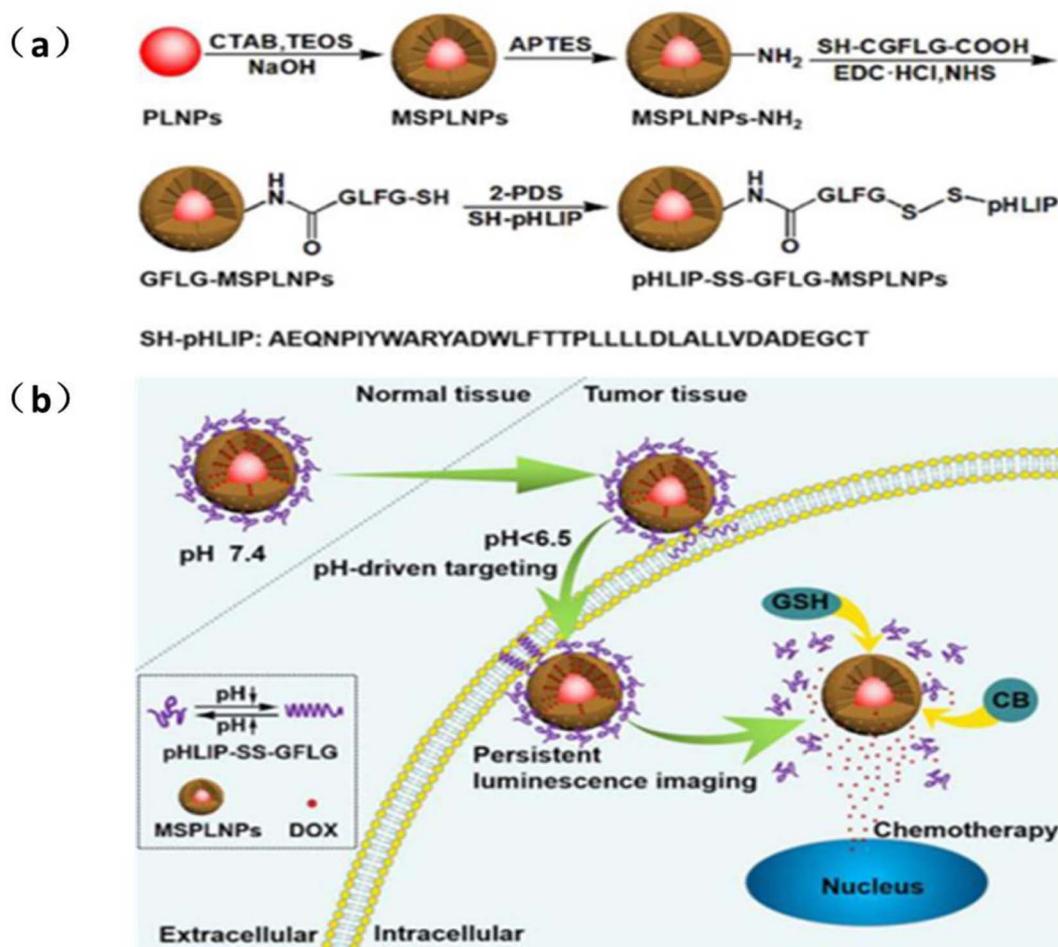
Fig. 13 (a) Design strategy and synthetic route of pH-LIP-SS-GFLG-MSPLNPs (b) schematic diagram of pH-LIP-SS-GFLG-MSPLNPs@DOX as a pH-driven targeted nanoprobe for the sustained luminescence imaging of tumors and chemotherapy. Reproduced from ref. 97 with permission from the American Chemical Society, copyright 2020.

persistent luminescence implant with stronger afterglow intensity and longer afterglow lifetime than $ZnGa_{1.996}O_4$:-$Cr_{0.004}$(ZGC) PLNPs, which can be repeatedly charged with LED for deep tissue afterglow imaging and PDT therapy greatly improving the therapeutic effect. Abdurahman et al.[189] reported that the combination of a photosensitizer (Si-Pc) and an 808 nm NIR-persistent luminescent material can provide an internal light source to generate singlet oxygen for photodynamic therapy without continuous external light source irradiation. In 2018, Liu et al.[190] composed $ZnGa_{1.996}O_4$:$Cr_{0.004}$ (PLNPs) and photosensitizer IR780 into temperature-responsive "wax-seal" therapeutic nanoplatforms. When activated by thermal stimulation, PLNPs can not only serve as an internal light source to continuously excite photosensitizers and generate reactive oxygen species, but also provide high-resolution imaging of cancer (Fig. 15).

4.3.5 Gene therapy. Gene therapy is a new type of cancer treatment that introduces exogenous normal genes into the target cells to correct or compensate for diseases caused by defective and abnormal genes for therapeutic purposes. This method has high specificity and effectiveness and fewer side

effects in post-surgical recovery.[191–193] Wu et al.[107] placed the therapeutic plasmid on polyetherimide (PEI) to modify PLNPs. A dual-functional persistent luminescent nanocomposite (LPLNP) was prepared, which was used for effective luminescence while tracking the homing and gene therapy of engineered mesenchymal stem cells (MSCs) glioblastoma (Fig. 16a and b). Qin et al.[194] designed and synthesized a local therapeutic system consisting of gold nanorods (Au NRs) loaded with TERT siRNA on the surface of $ZnGa_2O_4$:Cr (ZGOC) nanofibers. It amplified gene phagocytosis, siRNA release in the cytoplasm of the host Au NRs, and silencing effects through a potential LED-induced mild photothermal effect.

4.3.6 Combination therapy. In recent years, a new type of treatment called combination therapy has been developed. Combination therapy is a treatment that combines two or more therapies to treat cancer, such as the combination of surgical treatment, chemotherapy, photothermal, and photodynamic therapy. A variety of different combination therapies have been reported. Zhao et al.[195] reported acid-activated NIR PLNPs, which were endowed with tumor targeting and prolonged blood circulation under the surface functionalization of polyethylene
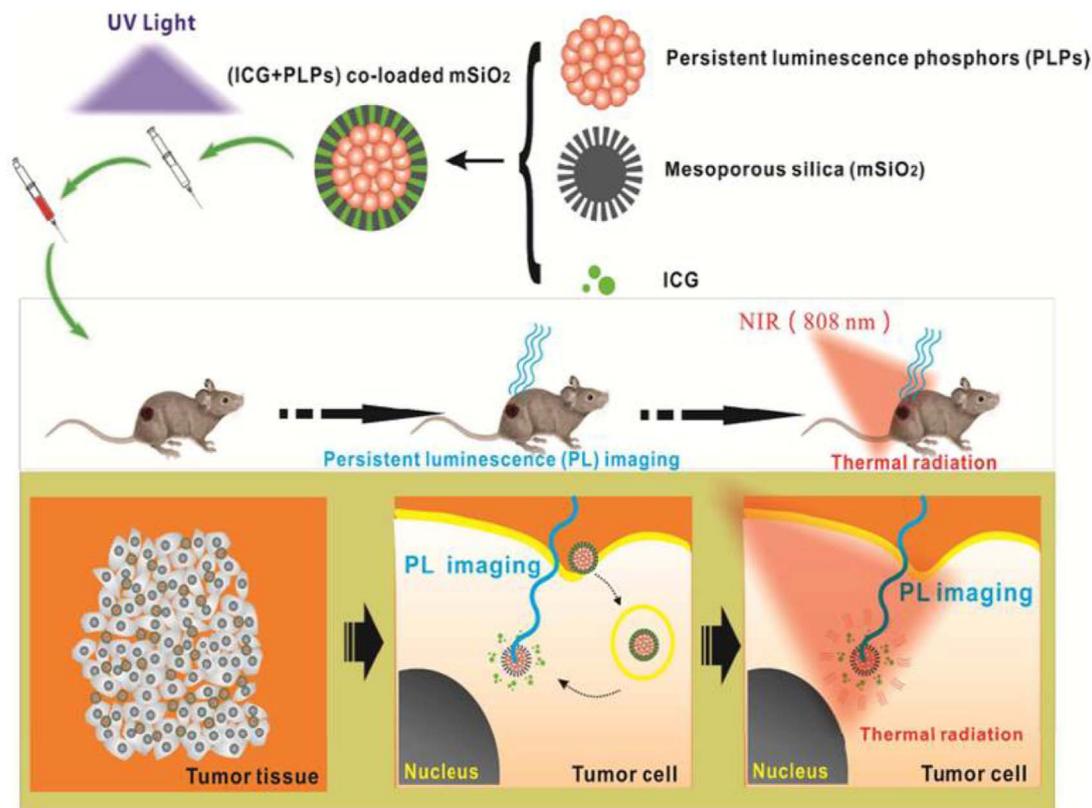
Fig. 14 Continuous luminescence imaging-guided *in vivo* PTT application of (ICG+PLPs)@mSiO$_2$ is depicted in this diagram. The schematic depicts the drug system's composition, which was injected into mice after UV excitation and guided *in vivo* PTT for cancer treatment using continuous luminescence imaging that tracked the drug's aggregation and diffusion *in vivo*. Reproduced from ref. 99 with permission from the American Chemical Society, copyright 2016.
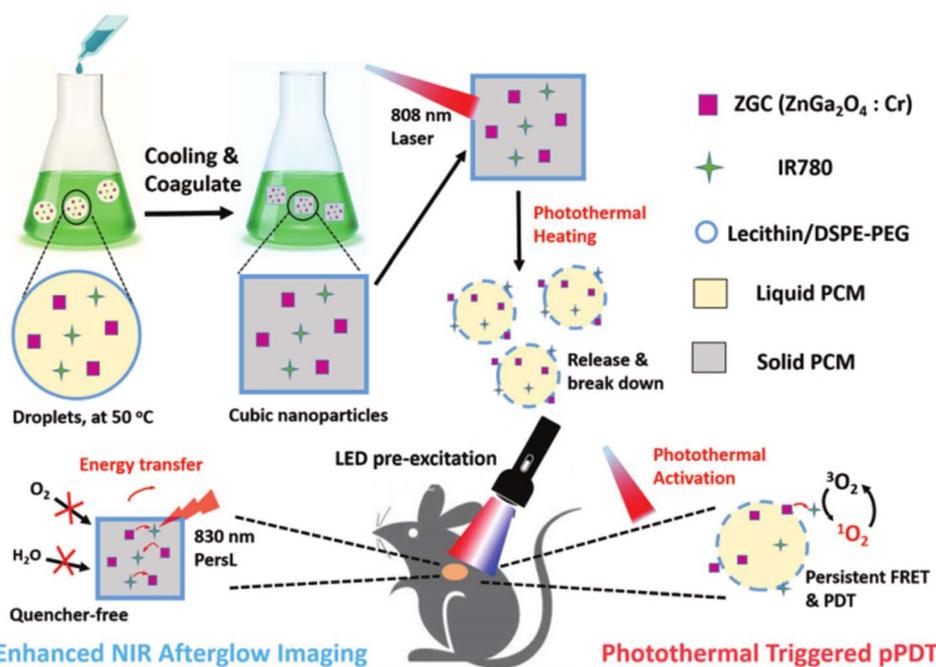

Fig. 15 Design of the "wax-seal" design of the IR-ZGC nanoplatform. Reproduced from ref. 190 with permission from Wiley-VCH, copyright 2018.
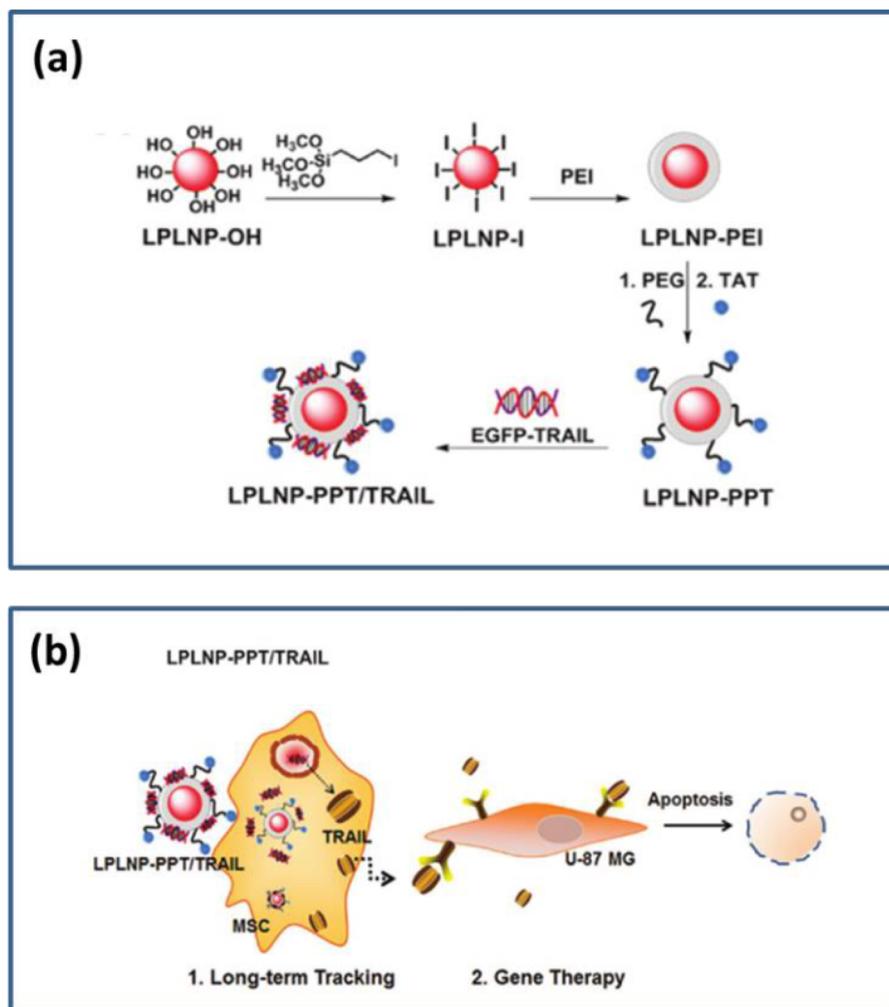
Fig. 16 (a) Schematic diagram of a surface functional modification of LPLNP (b) Schematic diagram of cell tracking and gene therapy. Reproduced from ref. 107 with permission from Wiley-VCH, copyright 2017.
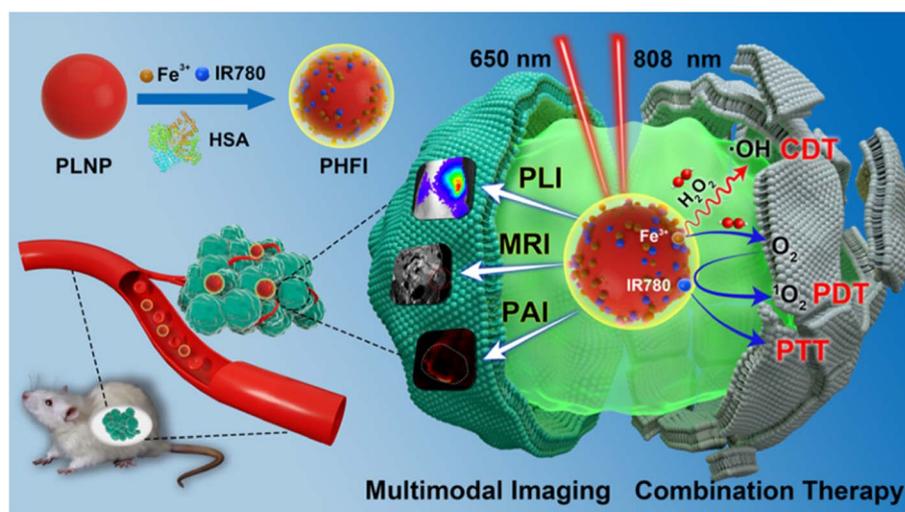

Fig. 17 Schematic of multimodality imaging and combination therapy. Reproduced from ref. 183 with permission from Wiley-VCH, copyright 2017.

glycol. Combined with the long-persistence properties of the material, the long-persistence imaging of tumors and the combined treatment of PTT/PDT are realized. Wu *et al.*[183] designed a multifunctional persistent luminescent nanoplatform (PHF) with human serum albumin (HSA) combined with an IR780 probe and Fe^{3+} modified near-infrared emitting persistent luminescent nanoparticles (PLNP), which can be used for multimodal imaging of tumors and also enabling Fenton-like combined photodynamic and photothermal therapy that can effectively overcome harsh treatment conditions to kill tumor cells (Fig. 17), demonstrating that the multifunctional persistent luminescent nanoplatform has great potential for cancer therapy.

5. Summary and outlook

In this review, we systematically summarize the luminescence mechanism, synthesis methods, and biomedical applications of NIR LPPs. As a promising alternative to traditional fluorescent materials, NIR LPPs have received widespread attention in the biomedical field because of their unique NIR afterglow characteristics. NIR LPPs can separate excitation and emission in time while avoiding background interference from fluorescence and scattered light. The most important one is that the emission range is in the NIR region. It has strong biological tissue penetration, high resolution and sensitivity, small absorption, and less scattering, which provides great convenience for its application in the biomedical field. Even though NIR LPPs have made significant growth in recent years, further work is required, including but not limited to:

(i) Synthesis method. At present, many synthesis methods have been reported, among which traditional synthesis methods include the high-temperature solid phase reaction method, combustion method, co-precipitation method, template method, and hydrothermal synthesis method. Based on the traditional synthesis method, electrostatic spinning, gas deposition, and electrospray pyrolysis are discovered, as well as a synthesis process that is helped by current technical methods such as microwave and ultrasound. Nevertheless, none of these synthesis methods is the best. It cannot simultaneously meet the requirements of morphological appearance, uniformity, and afterglow properties of NIR long afterglow materials, but only improves one or several of these properties. The most desirable synthesis method is that NIR LPPs with excellent morphology, homogeneity, afterglow properties, good stability, biocompatibility, recyclability, and low or even no toxicity can be synthesized by simple operations. At the same time, few or no pollutants are produced during the reaction. Therefore, the synthesis method needs further research.

(ii) Material Design. The design of materials includes two aspects. One is the design of the material itself, and the other is the design of the material after synthesis and before biological application. First of all, the design of the material itself refers to the design of the material synthesis. At present, the main thing is to choose some transition metal ions or rare earth ions as the luminescent center of the material when synthesizing the material, so as to achieve the purpose of improving the

afterglow performance of the material. At the same time, the degradability of the material should also be considered, which greatly contributes to the biosafety of the material. In 2020, Lecuyer *et al.*[196] demonstrated the degradability of ZGC in a lysosome-like medium following *in vivo* application in a simulated cellular environment, providing safety and credibility for the use of ZGC in the biomedical field. In addition, most of the currently reported NIR LPPs are focused on NIR-I. Fewer studies have been conducted in the NIR-II/III region, which has better tissue penetration and imaging capabilities, a strong investment in the research of NIR-II/III region luminescent materials is needed. The second is that after the material is synthesized, some materials with good biocompatibility are usually selected for functionalization and modification. This not only can improve the drug delivery and biocompatibility of the material but also can reduce the damage of the material itself to the organism. However, there are still a limited number of applications. Polyethylene glycol, folic acid, and other substances are available. Better, more functionalized modification materials are still in the works.

(iii) Excitation light. Excitation light is one of the most important factors for the afterglow properties of NIR LPPs, but most of the current applications involve UV excitation, and the afterglow time of the excited materials is not sufficient to support biological applications, requiring multiple repeated excitations. Therefore, future research on excitation light will focus on NIR light, radiation, and X-rays to better develop LPPs with NIR-II/III region luminescence.

(iv) Luminescence mechanism. Many different luminescence mechanisms have been reported, among which the most applied is the carrier model. No luminescence mechanism can be widely accepted by the general public yet. The luminescence properties of NIR LPPs are related to the type and depth of the traps present in the material and their ability to trap electrons. The study of the luminescence mechanism of the material also means the study of how the traps exist in the material and how the traps trap and release electrons during the luminescence process. Therefore, it is necessary to study how traps are involved in the luminescence process.

(v) Biological applications. There are three main applications of NIR LPPs in the biomedical field. They are biosensing detection, bioimaging, and cancer therapy. Among these, biosensing detection and cancer therapy are realized with the help of bioimaging technology. Breakthroughs in bioimaging technology have been achieved. With the guidance of bioimaging, the material and the drug combination system can now be applied to chemotherapy, PTT, PDT, gene therapy, and combination therapy. Despite the great progress in the research of NIR LPPs in the biomedical field, there is still a lack of experience in the research of these materials in clinical trials, mainly focusing on laboratory studies. Therefore, the biggest challenge of NIR LPPs in the biomedical field is the transition from laboratory research to clinical trials. Therefore, a bioapplication system for NIR LPPs should be constructed, so as to achieve efficient targeted drug transport, enable sufficient internalization of drugs in cells and tissues, promote the clinicalization of NIR LPPs, and make NIR LPPs better available for the biomedical field.

In conclusion, NIR LPPs are still in their initial stage of research. In the future development, NIR LPPs with better afterglow properties and application potential may emerge. We have to focus on the luminescence mechanism of this material and have a very in-depth luminescence mechanism in order to better build on the strengths and avoid the weaknesses, and design and synthesize NIR LPPs with better afterglow properties for better application potential in the biomedical field. We also believe that achieving this goal is very interesting and worthy of our expectations.

Conflicts of interest

There are no conflicts to declare.

Acknowledgements

References

1 Y. Liu, J. Kuang, B. Lei and C. Shi, *J. Mater. Chem. A*, 2005, **15**, 4025–4031.

2 Z. Pan, Y. Y. Lu and F. Liu, *Nat. Mater.*, 2011, **11**, 58–63.

3 Y. Wu, Y. Li, X. Qin and J. Qiu, *Chem.–Asian J.*, 2016, **11**, 2537–2541.

4 X. Chen, Y. Li, K. Huang, L. Huang, X. Tian, H. Dong, R. Kang, Y. Hu, J. Nie, J. Qiu and G. Han, *Adv. Mater.*, 2021, **33**, e2008722.

5 H. Jorma, *Electrochem. Soc. Interface*, 2009, **18**, 42–45.

6 J. Xu, J. Ueda and S. Tanabe, *J. Am. Ceram. Soc.*, 2017, **100**, 4033–4044.

7 Y. A. Matsuzawa, N. Takeuchi and Y. Murayama, *J. Electrochem. Soc.*, 1996, **143**, 2670–2673.

8 R. E. Rojas-Hernandez, F. Rubio-Marcos, M. A. Rodriguez and F. F. Jose, *Renewable Sustainable Energy Rev.*, 2018, **81**, 2759–2770.

9 C. Chanéac, Q. l. M. d. Chermont, J. Seguin, F. Pelle, S. Maîtrejean, J.-P. Jolivet, D. Gourier, M. Bessodes and D. Scherman, *Proc. Natl. Acad. Sci., India, Sect. B*, 2007, **104**, 9266–9271.

10 N. Liu, J. Shi, Q. Wang, J. Guo, Z. Hou, X. Su, H. Zhang and X. Sun, *Small*, 2020, **16**, e2001494.

11 L. Liang, N. Chen, Y. Jia, Q. Ma, J. Wang, Q. Yuan and W. J. N. R. Tan, *Nano Res.*, 2019, **12**, 1279–1292.

12 Z. Xue, X. Li, Y. Li, M. Jiang, G. Ren, H. Liu, S. Zeng and J. Hao, *Nanoscale*, 2017, **9**, 7276–7283.

13 Y. Zhuang, D. Chen, W. Chen, W. Zhang, X. Su, R. Deng, Z. An, H. Chen and R. J. Xie, *Light: Sci. Appl.*, 2021, **10**, 132–142.

14 X. Ou, X. Qin, B. Huang, J. Zan, Q. Wu, Z. Hong, L. Xie, H. Bian, Z. Yi, X. Chen, Y. Wu, X. Song, J. Li, Q. Chen, H. Yang and X. Liu, *Nature*, 2021, **590**, 410–415.

15 P. Pei, Y. Chen, C. Sun, Y. Fan, Y. Yang, X. Liu, L. Lu, M. Zhao, H. Zhang, D. Zhao, X. Liu and F. Zhang, *Nat. Nanotechnol.*, 2021, **16**, 1011–1018.

16 B. Hou, Y. Cho, B. S. Kim, D. Ahn, S. Lee, J. B. Park, Y. W. Lee, J. Hong, H. Im, S. M. Morris, J. I. Sohn, S. Cha and J. M. Kim, *J. Mater. Chem. C*, 2017, **5**, 3692–3698.

17 B. Paul, S. Maiti, T. Paul, B. Chatterjee, S. Maiti, S. Sarkar, N. Besra, B. Das, K. Panigrahi, S. Thakur, U. Ghorai and K. Chattopadhyay, *J. Mater. Chem. C*, 2018, 11374–11383.

18 J. Ueda, J. L. Leaño, C. Richard, K. Asami, S. Tanabe and R.-S. Liu, *J. Mater. Chem. C*, 2019, **7**, 1705–1712.

19 J. Xu, D. Murata, J. Ueda, B. Viana and S. Tanabe, *Inorg. Chem.*, 2018, **57**, 5194–5203.

20 J. Yu, M. Luo, Z. Lv, S. Huang, H. H. Hsu, C. C. Kuo, S. T. Han and Y. Zhou, *Nanoscale*, 2020, **12**, 23391–23423.

21 H. Tan, T. Wang, Y. Shao, C. Yu and L. Hu, *Front. Chem.*, 2019, **7**, 387.

22 J. Wang, Q. Ma, Y. Wang, H. Shen and Q. Yuan, *Nanoscale*, 2017, **9**, 6204–6218.

23 T. L. Jianhua Liu, J. Séguin, N. Mignet, D. Scherman, B. Viana and C. Richard, *Adv. Drug Delivery Rev.*, 2019, **138**, 193–210.

24 B. Viana, S. Sharma, D. Gourier, T. Maldiney, E. Teston, D. Scherman and C. Richard, *J. Lumin.*, 2016, 879–887.

25 L. Liang, N. Chen, Y. Jia, Q. Ma, J. Wang, Q. Yuan and W. Tan, *Nano Res.*, 2019, **12**, 1279–1292.

26 G. Su, R. Shen, J. Tan and Q. Yuan, *Chem. J. Chin. Univ.*, 2020, **41**, 2404–2414.

27 J. M. Ortega and M. Roncel, *Physiol. Plant.*, 2021, **171**, 268–276.

28 B. Qu, J. Wang, K. Liu, R. Zhou and L. Wang, *Phys. Chem. Chem. Phys.*, 2019, **21**, 25118–25125.

29 S. Jiang, M. J. F. Digonnet, M. Pellerin, C. Coelho-Diogo, C. Bonhomme, N. Touatib, L. Binet, D. Gourier, J. Ueda, S. Tanabe, B. Viana and C. Chanéac, *Opt. Compon. Mater. XIV*, 2017, **10100**, 46–52.

30 N. Majewska, T. Lesniewski, S. Mahlik, M. Grinberg, A. Chruscinska, D. Michalik and M. Sopicka-Lizer, *Phys. Chem. Chem. Phys.*, 2020, **22**, 17152–17159.

31 A. J. J. Bos, *Materials*, 2017, **10**, 1357–1379.

32 J. H. o. a. Tuomas Aitasalo, H. ogne Jungner, M. Lastusaari and J. Niittykoski, *J. Lumin.*, 2001, **94**, 59–63.

33 A. Zhang, C. Huang, H. Shi, W. Guo, X. Zhang, H. Xiang, T. Jia, F. Miao and N. Jia, *Sens. Actuators, B*, 2017, **238**, 24–31.

34 K. M. Jianrong Qiu a, H. Inouye, S. Fujiwara, T. Mitsuyu and K. Hirao, *J. Non-Cryst. Solids*, 1999, **244**, 185–188.

35 Q. S. Tianzhi Zhang and S. Wang, *Chinese J. Lumin.*, 1999, **20**, 170–175.

36 W. Zhao, T. S. Cheung, N. Jiang, W. Huang, J. W. Y. Lam, X. Zhang, Z. He and B. Z. Tang, *Nat. Commun.*, 2019, **10**, 1595.

37 L. Gu, H. Shi, L. Bian, M. Gu, K. Ling, X. Wang, H. Ma, S. Cai, W. Ning, L. Fu, H. Wang, S. Wang, Y. Gao, W. Yao, F. Huo, Y. Tao, Z. An, X. Liu and W. Huang, *Nat. Photonics*, 2019, **13**, 406–411.

38 V. Abbruscato, *J. Electrochem. Soc.*, 1971, **118**, 930–933.

39 T. M. Kyota Uheda, H. Takizawa and T. Endo, *J. Alloys Compd.*, 1997, **262**, 60–64.

40 W. Sun, R. Pang, H. Li, D. Li, L. Jiang, S. Zhang, J. Fu and C. Li, *J. Mater. Chem. C*, 2017, **5**, 1346–1355.

41 W. Hoogenstraaten, *Philips Res. Rep.*, 1958, **13**, 515–693.

42 I. F. Chang and P. Thioulouse, *J. Appl. Phys.*, 1982, **53**, 5873–5875.

43 W. Chen, S. Zhang, M. Zhou, T. Zhao, X. Qin, X. Liu, M. Liu and P. Duan, *J. Phys. Chem. Lett.*, 2019, **10**, 3290–3295.

44 Y. Dou, Q. Zhu and K. Du, *Chembiochem*, 2021, **22**, 1871–1883.

45 X. Dai, X. Zhang, I. M. Kislyakov, L. Wang, J. Huang, S. Zhang, N. Dong and J. Wang, *Opt. Express*, 2019, **27**, 13744–13753.

46 Y. Zhao, H. Zeng, X. W. Zhu, W. Lu and D. Li, *Chem. Soc. Rev.*, 2021, **50**, 4484–4513.

47 Y. Cui, Y. Yue, G. Qian and B. Chen, *Chem. Rev.*, 2012, **112**, 1126–1162.

48 Y. Cui, J. Zhang, H. He and G. Qian, *Chem. Soc. Rev.*, 2018, **47**, 5740–5785.

49 J. Heine and K. Muller-Buschbaum, *Chem. Soc. Rev.*, 2013, **42**, 9232–9242.

50 Y. Ning, G. Q. Jin, M. X. Wang, S. Gao and J. L. Zhang, *Curr. Opin. Chem. Biol.*, 2022, **66**, 102097.

51 L. Zhao, X. Song, X. Ren, H. Wang, D. Fan, D. Wu and Q. Wei, *Biosens. Bioelectron.*, 2021, **191**, 113409.

52 H. Xu, W. Yu, K. Pan, G. Wang and P. Zhu, *Nano Res.*, 2020, **14**, 720–729.

53 W. Shang, X. Zhu, T. Liang, C. Du, L. Hu, T. Li and M. Liu, *Angew. Chem., Int. Ed. Engl.*, 2020, **59**, 12811–12816.

54 A. Halder, B. Bhattacharya, F. Haque, S. Dinda and D. Ghoshal, *Chem*, 2019, **25**, 12196–12205.

55 C. Y. Liu, X. R. Chen, H. X. Chen, Z. Niu, H. Hirao, P. Braunstein and J. P. Lang, *J. Am. Chem. Soc.*, 2020, **142**, 6690–6697.

56 D. J. Vogel, T. M. Nenoff and J. M. Rimsza, *ACS Appl. Mater. Interfaces*, 2020, **12**, 4531–4539.

57 M. Zeng, C. Zhan and J. Yao, *J. Mater. Chem. C*, 2019, **7**, 2751–2757.

58 X. Feng, PhD thesis, Tianjin Polytech. Univ., 2021.

59 T. Lyu and P. Dorenbos, *J. Mater. Chem. C*, 2018, **6**, 369–379.

60 J. Xu, D. Murata, Y. Katayama, J. Ueda and S. Tanabe, *J. Mater. Chem. B*, 2017, **5**, 6385–6393.

61 S. Kamimura, C.-N. Xu, H. Yamada, G. Marriott, K. Hyodo and T. Ohno, *J. Ceram. Soc. Jpn.*, 2017, **125**, 591–595.

62 S. Lin, H. Lin, C. Ma, Y. Cheng, S. Ye, F. Lin, R. Li, J. Xu and Y. Wang, *Light: Sci. Appl.*, 2020, **9**, 22.

63 D. C. Rodríguez Burbano, S. K. Sharma, P. Dorenbos, B. Viana and J. A. Capobianco, *Adv. Opt. Mater.*, 2015, **3**, 551–557.

64 P. Xiong and M. Peng, *J. Mater. Chem. C*, 2019, **7**, 8303–8309.

65 F. Liu, Y. Liang, Y. Chen and Z. Pan, *Adv. Opt. Mater.*, 2016, **4**, 562–566.

66 C. Ma, H. Liu, F. Ren, Z. Liu, Q. Sun, C. Zhao and Z. Li, *Cryst. Growth Des.*, 2020, **20**, 1859–1867.

67 Z. Zou, C. Wu, X. Li, J. Zhang, H. Li, D. Wang and Y. Wang, *Opt. Lett.*, 2017, **42**, 4510–4512.

68 M. Pellerin, V. Castaing, D. Gourier, C. Chanéac and B. Viana, *Oxide-based Mater. Devices IX.SPIE*, 2018, **10533**, 196–203.

69 J. Xu, S. Tanabe, A. D. Sontakke and J. Ueda, *Appl. Phys. Lett.*, 2015, **107**, 081903.

70 J. Xu, D. Murata, B. So, K. Asami, J. Ueda, J. Heo and S. Tanabe, *J. Mater. Chem. C*, 2018, **6**, 11374–11383.

71 Y. Chen, J. Duh, B. Chiou and C. Peng, *Thin Solid Films*, 2001, **392**, 50–55.

72 Z. Gong, W. Zheng, Y. Gao, P. Huang, D. Tu, R. Li, J. Wei, W. Zhang, Y. Zhang and X. Chen, *Angew. Chem., Int. Ed. Engl.*, 2019, **58**, 6943–6947.

73 P. Zhang, M. Xu, Z. Zheng, B. Sun and Y. Zhang, *Mater. Sci. Eng., B*, 2007, **136**, 159–164.

74 J. Du, O. Q. De Clercq, K. Korthout and D. Poelman, *Materials*, 2017, **10**, 1422.

75 S. Li, Q. Zhu, X. Li, X. Sun and J.-G. Li, *J. Alloys Compd.*, 2020, **827**, 154365.

76 Y. Katayama, *J. Ceram. Soc. Jpn.*, 2017, **125**, 793–798.

77 J. C. G. Bünzli, *Eur. J. Inorg. Chem.*, 2017, **2017**, 5058–5063.

78 T. Maldiney, B. Ballet, M. Bessodes, D. Scherman and C. Richard, *Nanoscale*, 2014, **6**, 13970–13976.

79 T. Luan, J. Liu, X. Yuan and J. G. Li, *Nanoscale Res. Lett.*, 2017, **12**, 219.

80 S. J. Aurélie Bessière, K. Priolkar, A. Lecointre, B. Viana and D. Gourier, *Opt. Express*, 2011, **19**, 10131–10137.

81 Z. Zhou, W. Zheng, J. Kong, Y. Liu, P. Huang, S. Zhou, Z. Chen, J. Shi and X. Chen, *Nanoscale*, 2017, **9**, 6846–6853.

82 Y. Liu, Y. Wang, K. Jiang, S. Sun, S. Qian, Q. Wu and H. Lin, *Talanta*, 2020, **206**, 120206.

83 T. Maldiney, A. Bessiere, J. Seguin, E. Teston, S. K. Sharma, B. Viana, A. J. Bos, P. Dorenbos, M. Bessodes, D. Gourier, D. Scherman and C. Richard, *Nat. Mater.*, 2014, **13**, 418–426.

84 X. H. Lin, L. Song, S. Chen, X. F. Chen, J. J. Wei, J. Li, G. Huang and H. H. Yang, *ACS Appl. Mater. Interfaces*, 2017, **9**, 41181–41187.

85 T. Maldiney, B.-T. Doan, D. Alloyeau, M. Bessodes, D. Scherman and C. Richard, *Adv. Funct. Mater.*, 2015, **25**, 331–338.

86 E. Teston, Y. Lalatonne, D. Elgrabli, G. Autret, L. Motte, F. Gazeau, D. Scherman, O. Clement, C. Richard and T. Maldiney, *Small*, 2015, **11**, 2696–2704.

87 E. Glais, M. Pellerin, V. Castaing, D. Alloyeau, N. Touati, B. Viana and C. Chanéac, *RSC Adv.*, 2018, **8**, 41767–41774.

88 H. Yang, W. Zhao, X. Lin, Z. Liao, Z. Nie, L. Luo, W. Zhang, Z. Hu and J. Zhong, *J. Lumin.*, 2020, **219**, 116871.

89 J. Shi, X. Sun, S. Zheng, J. Li, X. Fu and H. Zhang, *Biomater*, 2018, **152**, 15–23.

90 P. Sengar, D.-L. Flores, K. Chauhan, B. Can-Uc, K. Juarez-Moreno, O. E. Contreras, M. A. Digman and G. A. Hirata, *Cryst. Growth Des.*, 2020, **20**, 5880–5889.

91 B. L. Yan Cong, S. Yue, L. Zhang, W. Li and X.-j. Wang, *J. Electrochem. Soc.*, 2009, **154**, H272–H275.

92 X. Wang, J. Ding and Y. Wang, *J. Mater. Chem. C*, 2018, **6**, 7353–7360.

93 L. J. Chen, X. Zhao and X. P. Yan, *ACS Appl. Mater. Interfaces*, 2019, **11**, 19894–19901.

94 J. Wang, Q. Ma, X. X. Hu, H. Liu, W. Zheng, X. Chen, Q. Yuan and W. Tan, *ACS Nano*, 2017, **11**, 8010–8017.

95 L. Chen, C. Yang and X. Yan, *Anal. Chem.*, 2017, **13**, 6936–6939.

96 J. Shi, X. Sun, J. Li, H. Man, J. Shen, Y. Yu and H. Zhang, *Biomater*, 2015, **37**, 260–270.

97 H. J. Zhang, X. Zhao, L. J. Chen, C. X. Yang and X. P. Yan, *Anal. Chem.*, 2020, **92**, 1179–1188.

98 J. M. Liu, D. D. Zhang, G. Z. Fang and S. Wang, *Biomater*, 2018, **165**, 39–47.

99 B. Zheng, H. B. Chen, P. Q. Zhao, H. Z. Pan, X. L. Wu, X. Q. Gong, H. J. Wang and J. Chang, *ACS Appl. Mater. Interfaces*, 2016, **8**, 21603–21611.

100 L. Huang, L. Lin, W. Xie, Z. Qiu, H. Ni, H. Liang, Q. Tang, L. Cao, J. Meng and F. Li, *Chem. Mater.*, 2020, **32**, 5579–5588.

101 X. Qin, Y. Li, D. Wu, Y. Wu, R. Chen, Z. Ma, S. Liu and J. Qiu, *RSC Adv.*, 2015, **5**, 101347–101352.

102 Y. Ning, S. Cheng, J. Wang, X. Liu, Y. Feng, W. Li and J. Zhang, *R. Soc. Chem.*, 2019, **10**, 4227–4235.

103 M. Palner, K. Pu, S. Shao and J. Rao, *Angew. Chem., Int. Ed. Engl.*, 2015, **54**, 11477–11480.

104 Q. Miao, C. Xie, X. Zhen, Y. Lyu, H. Duan, X. Liu, J. V. Jokerst and K. Pu, *Nat. Biotechnol.*, 2017, **35**, 1102–1110.

105 X. Ni, X. Zhang, X. Duan, H. L. Zheng, X. S. Xue and D. Ding, *Nano Lett.*, 2019, **19**, 318–330.

106 L. Lu, B. Li, S. Ding, Y. Fan, S. Wang, C. Sun, M. Zhao, C. X. Zhao and F. Zhang, *Nat. Commun.*, 2020, **11**, 4192–4203.

107 S. Wu, C. Yang and X. Yan, *Adv. Funct. Mater.*, 2017, **27**, 1604992.

108 J. Nie, Y. Li, S. Liu, Q. Chen, Q. Xu and J. Qiu, *Sci. Rep.*, 2017, **7**, 12392.

109 Y. Lin, J. Hu, L. Wu, Q. Zou, D. Chen, D. Huang, H. Lu, S. B. Wang and H. Zhu, *J Mater Chem B*, 2021, **9**, 1131–1137.

110 R. Cao, X. Yu, X. Sun, C. Cao and J. Qiu, *Spectrochim. Acta. A. Mol. Biomol. Spectrosc.*, 2014, **128**, 671–673.

111 K. Huang, N. Le, J. S. Wang, L. Huang, L. Zeng, W. C. Xu, Z. Li, Y. Li and G. Han, *Adv. Mater.*, 2022, **34**, 2107962.

112 O. Hai, M. Pei, E. Yang, Q. Ren, X. Wu, J. Zhu, Y. Zhao and L. Du, *J. Alloys Compd.*, 2021, **866**, 158752.

113 C. L. Wu, *Mod. Chem. Ind.*, 2019, **39**, 197–202.

114 G. Qi, PhD thesis, North China Electr. Power Univ., 2018.

115 L. Sun, Q. Wang, X. Lin and J. Zhou, *J. Shandong Univ. Sci. Technol.*, 2012, **31**, 74–80.

116 N. Zhang, C. G. Liu, M. Zhang, J. Yang, S. N. Li, H. C. Zhu, D. T. Yan, C. S. Xu and Y. X. Liu, *Spectrosc. Spect. Anal.*, 2020, **40**, 373–378.

117 L. Ni, M. Wang, Z. X. Zhu, M. Li, C. A. J. Yuan and J. Wu, *Chin. J. Anal. Chem.*, 2022, **50**, 103–111.

118 X. Wei, X. Huang, Y. Zeng, L. Jing, W. Tang, X. Li, H. Ning, X. Sun, Y. Yi and M. Gao, *ACS Nano*, 2020, **14**, 12113–12124.

119 Z. Zhou, Y. Li and M. Peng, *Chem. Eng. J.*, 2020, **399**, 125688.

120 Y. Yang, H. Pan, L. Guan, D. Wang, J. Zhao, J. Yang, Z. Yang and X. Li, *J. Mater. Res. Technol.*, 2020, **9**, 3847–3855.

121 P. Ankoji and B. H. Rudramadevi, *J. Mater. Sci.: Mater. Electron.*, 2018, **30**, 2750–2762.

122 Y. Wang, S. Chen and L. Geng, *J. Rare Earths*, 2021, **39**, 913–920.

123 L. Pan, S. Liu, X. Zhang, O. Oderinde, F. Yao and G. Fu, *J. Alloys Compd.*, 2018, **737**, 39–45.

124 J. H. Lee, C. K. Yun, B. P. Seung and P. Hee Dong, *Jpn. Soc. Appl. Phys.*, 2001, **40**, 4083–4086.

125 Y. C. Kang, D. J. Seo, S. B. Park and H. D. Park, *Mater. Res. Bull.*, 2002, **37**, 263–269.

126 Z. Li, Y. Zhang, X. Wu, C. Qin and G. Shi, *Phys. Lett. A*, 2017, **381**, 3519–3522.

127 Z. Marton, H. B. Bhandari, C. Brecher, S. R. Miller, B. Singh and V. V. Nagarkar, *IEEE Trans. Nucl. Sci.*, 2013, **60**, 983–987.

128 G. Dong, X. Xiao, L. Zhang, Z. Ma, X. Bao, M. Peng, Q. Zhang and J. Qiu, *J. Mater. Chem.*, 2011, **21**, 2194–2203.

129 F. Ye, S. Dong, Z. Tian, S. Yao, Z. Zhou and S. Wang, *Opt. Mater.*, 2015, **45**, 64–68.

130 A. A. Tehrani, V. Safarifard, A. Morsali, G. Bruno and H. A. Rudbari, *Inorg. Chem. Commun.*, 2015, **59**, 41–45.

131 M. Y. Masoomi, A. Morsali and P. C. Junk, *RSC Adv.*, 2014, **4**, 47894–47898.

132 Y. Jin, Y. Fu, Y. Hu, L. Chen, G. Ju and Z. Mu, *Opt. Mater. Express*, 2015, **3**, 9435–9443.

133 B. Cheng, Z. Zhang, Z. Han, Y. Xiao and S. Lei, *CrystEngComm*, 2011, **13**, 3545–3550.

134 B. Zhang, C. Zhao and D. Chen, *Lumin*, 2010, **25**, 25–29.

135 S. Demirci, S. Gültekin, S. A. Akalin, Ö. Öter, K. Ertekin and E. Çelik, *Mater. Sci. Semicond. Process.*, 2015, **31**, 611–617.

136 E. Teston, S. Richard, T. Maldiney, N. Lièvre, G. Y. Wang, L. Motte, C. Richard and Y. J. C. A. E. J. Lalatonne, *Chem*, 2015, **21**, 7350–7354.

137 C. Matias, E. Nassar, M. Verelst and L. Rocha, *J. Braz. Chem. Soc.*, 2015, **26**, 2558–2570.

138 D. Meroni, L. Porati, F. Demartin and D. Poelman, *ACS Omega*, 2017, **2**, 4972–4981.

139 J. Yang, Y. Liu, D. Yan, H. Zhu, C. Liu, C. Xu, L. Ma and X. Wang, *Dalton Trans.*, 2016, **45**, 1364–1372.

140 M. Xia, G. Wang, Z. Gu, Z. Qiu, C. Rong, J. Zhang, W. Zhou, L. Yu and S. Lian, *Luminescence*, 2017, **32**, 999–1008.

141 Y. J. Li and X. P. Yan, *Nanoscale*, 2016, **8**, 14965–14970.

142 M. Pellerin, E. Glais, T. Lecuyer, J. Xu, J. Seguin, S. Tanabe, C. Chanéac, B. Viana and C. Richard, *J. Lumin.*, 2018, **202**, 83–88.

143 V. Boiko, M. Markowska, L. Consentino, M. L. Saladino and D. Hreniak, *Opt. Mater.*, 2020, **107**, 109956.

144 Y. Liu, J. Goebl and Y. Yin, *Chem. Soc. Rev.*, 2013, **42**, 2610–2653.

145 Y. Oaki, *Supra-Materials Nanoarchitectonics*, 2017, **10**, 221–246.

146 Y. Zhang, Y. Su, H. Wu, Z. Wang, C. Wang, Y. Zheng, X. Zheng, L. Gao, Q. Zhou and Y. Yang, *J. Am. Chem. Soc.*, 2021, **143**, 13675–13685.

147 G. Nidhankar, D. Mohana Kumari, S. Kumar, R. Chaubey, R. Gonnade, G. Kumar, R. Krishnan and S. Babu, *Angew. Chem., Int. Ed.*, 2020, **59**, 13079–13085.

148 H. Chen, X. Yao, X. Ma and H. Tian, *Adv. Opt. Mater.*, 2016, **4**, 1397–1401.

149 C. DeRosa, C. Kerr, Z. Fan, M. Kolpaczynska, A. Mathew, R. Evans, G. Zhang and C. Fraser, *ACS Appl. Mater. Interfaces*, 2015, **7**, 23633–23643.

150 H. Shi, L. Song, H. Ma, C. Sun, K. Huang, A. Lv, W. Ye, H. Wang, S. Cai, W. Yao, Y. Zhang, R. Zheng, Z. An and W. Huang, *J. Phys. Chem. Lett.*, 2019, **10**, 595–600.

151 Z. An, C. Zheng, Y. Tao, R. Chen, H. Shi, T. Chen, Z. Wang, H. Li, R. Deng, X. Liu and W. Huang, *Nat. Mater.*, 2015, **14**, 685–690.

152 Y. Gong, G. Chen, Q. Peng, W. Z. Yuan, Y. Xie, S. Li, Y. Zhang and B. Z. Tang, *Adv. Mater.*, 2015, **27**, 6195–6201.

153 M. Shimizu, R. Shigitani, M. Nakatani, K. Kuwabara, Y. Miyake, K. Tajima, H. Sakai and T. Hasobe, *J. Phys. Chem. C*, 2016, **120**, 11631–11639.

154 J. Wang, X. Gu, H. Ma, Q. Peng, X. Huang, X. Zheng, S. H. P. Sung, G. Shan, J. W. Y. Lam, Z. Shuai and B. Z. Tang, *Nat. Commun.*, 2018, **9**, 2963.

155 H. Shi, Z. An, P.-Z. Li, J. Yin, G. Xing, T. He, H. Chen, J. Wang, H. Sun, W. Huang and Y. Zhao, *Cryst. Growth Des.*, 2016, **16**, 808–813.

156 S. Hirata, K. Totani, T. Watanabe, H. Kaji and M. Vacha, *Chem. Phys. Lett.*, 2014, **591**, 119–125.

157 N. Notsuka, R. Kabe, K. Goushi and C. Adachi, *Adv. Funct. Mater.*, 2017, **27**, 1703902.

158 S. Hirata, K. Totani, H. Kaji, M. Vacha, T. Watanabe and C. Adachi, *Adv. Opt. Mater.*, 2013, **1**, 438–442.

159 S. Cai, H. Shi, Z. Zhang, X. Wang, H. Ma, N. Gan, Q. Wu, Z. Cheng, K. Ling, M. Gu, C. Ma, L. Gu, Z. An and W. Huang, *Angew. Chem., Int. Ed. Engl.*, 2018, **57**, 4005–4009.

160 Z. Cheng, H. Shi, H. Ma, L. Bian, Q. Wu, L. Gu, S. Cai, X. Wang, W. W. Xiong, Z. An and W. Huang, *Angew. Chem., Int. Ed. Engl.*, 2018, **57**, 678–682.

161 M. S. Kwon, Y. Yu, C. Coburn, A. W. Phillips, K. Chung, A. Shanker, J. Jung, G. Kim, K. Pipe, S. R. Forrest, J. H. Youk, J. Gierschner and J. Kim, *Nat. Commun.*, 2015, **6**, 8947.

162 D. Lee, O. Bolton, B. C. Kim, J. H. Youk, S. Takayama and J. Kim, *J. Am. Chem. Soc.*, 2013, **135**, 6325–6329.

163 M. S. Kwon, D. Lee, S. Seo, J. Jung and J. Kim, *Angew. Chem., Int. Ed. Engl.*, 2014, **53**, 11177–11181.

164 J. Samonina-Kosicka, C. A. DeRosa, W. A. Morris, Z. Fan and C. L. Fraser, *Macromol*, 2014, **47**, 3736–3746.

165 Y. Tao, R. Chen, H. Li, J. Yuan, Y. Wan, H. Jiang, C. Chen, Y. Si, C. Zheng, B. Yang, G. Xing and W. Huang, *Adv. Mater.*, 2018, **30**, e1803856.

166 J. Jin, H. Jiang, Q. Yang, L. Tang, Y. Tao, Y. Li, R. Chen, C. Zheng, Q. Fan, K. Y. Zhang, Q. Zhao and W. Huang, *Nat. Commun.*, 2020, **11**, 842.

167 T. Maldiney, M. U. Kaikkonen, J. Seguin, Q. le Masne de Chermont, M. Bessodes, K. J. Airenne, S. Ylä-Herttuala, D. Scherman and C. Richard, *Bioconjugate Chem.*, 2012, **23**, 472–478.

168 B. Y. Wu, H. F. Wang, J. T. Chen and X. P. Yan, *J. Am. Chem. Soc.*, 2011, **133**, 686–688.

169 M. H. Ahmed, M. S. Ghatge and M. K. Safo, *Subcell. Biochem.*, 2020, **94**, 345–382.

170 X. Zhao, J. Zhou, G. Du and J. Chen, *Trends Biotechnol.*, 2021, **39**, 286–297.

171 B. Lin, X. Dong, Q. Wang, W. Li, M. Zhu and M. Li, *Front. Cell Dev. Biol.*, 2021, **9**, 635476.

172 F. Ozdemir and A. Baskiran, *J. Gastrointest. Cancer*, 2020, **51**, 1127–1132.

173 Q. Wang, S. Zhang, Z. Li and Q. Zhu, *Nanoscale Res. Lett.*, 2018, **13**, 64.

174 X. Sun, J. Shi, S. Zheng, J. Li, S. Wang and H. Zhang, *J. Lumin.*, 2018, **204**, 520–527.

175 K. Jeong, Y. Kim, C. S. Kang, H.-J. Cho, Y.-D. Lee, I. C. Kwon and S. Kim, *Opt. Mater. Express*, 2016, **6**, 1262–1280.

176 I. B. Alaya and M. Mars, *Curr. Med. Imaging*, 2020, **16**, 892–901.

177 S. Mule, E. Reizine, P. Blanc-Durand, L. Baranes, P. Zerbib, R. Burns, R. Nouri, E. Itti and A. Luciani, *Cancers*, 2020, **12**, 23391–23423.

178 Y. Wang, C. X. Yang and X. P. Yan, *Nanoscale*, 2017, **9**, 9049–9055.

179 J. Wang, Q. Li, H. Zhao, W. Yue, K. Zhang, X. Jiang and K. Li, *ACS Nano*, 2021, **16**, 462–472.

180 A. Abdukayum, C. X. Yang, Q. Zhao, J. T. Chen, L. X. Dong and X. P. Yan, *Anal. Chem.*, 2014, **86**, 4096–4101.

181 Y. Zhang, H. F. Chan and K. W. Leong, *Adv. Drug Delivery Rev.*, 2013, **65**, 104–120.

182 F. Chen, E. B. Ehlerding and W. Cai, *J. Nucl. Med.*, 2014, **55**, 1919–1922.

183 S. Wu, Z. Qiao, Y. Li, S. Hu, Y. Ma, S. Wei and L. Zhang, *ACS Appl. Mater. Interfaces*, 2020, **12**, 25572–25580.

184 S. Mura, J. Nicolas and P. Couvreur, *Nat. Mater.*, 2013, **12**, 991–1003.

185 H. Chen, B. Zheng, C. Liang, L. Zhao, Y. Zhang, H. Pan, W. Ji, X. Gong, H. Wang and J. Chang, *Mater. Sci. Eng., C*, 2017, **79**, 372–381.

186 J. Wang, Y. Li, R. Mao, Y. Wang, X. Yan and J. Liu, *J. Mater. Chem. B*, 2017, **5**, 5793–5805.

187 T. Ozdemir, Y.-C. Lu, S. Kolemen, E. Tanriverdi-Ecik and E. U. Akkaya, *ChemPhotoChem*, 2017, **1**, 183–187.

188 W. Fan, N. Lu, C. Xu, Y. Liu, J. Lin, S. Wang, Z. Shen, Z. Yang, J. Qu, T. Wang, S. Chen, P. Huang and X. Chen, *ACS Nano*, 2017, **11**, 5864–5872.

189 R. Abdurahman, C. X. Yang and X. P. Yan, *Chem. Commun.*, 2016, **52**, 13303–13306.

190 G. Liu, S. Zhang, Y. Shi, X. Huang, Y. Tang, P. Chen, W. Si, W. Huang and X. Dong, *Adv. Funct. Mater.*, 2018, **28**, 1804317.

191 S. K. Das, M. E. Menezes, S. Bhatia, X. Y. Wang, L. Emdad, D. Sarkar and P. B. Fisher, *J. Cell. Physiol.*, 2015, **230**, 259–271.

192 Z. Mirza and S. Karim, *Semin. Cancer Biol.*, 2021, **69**, 226–237.

193 E. B. Yahya and A. M. Alqadhi, *Life Sci.*, 2021, **269**, 119087.

194 L. Qin, P. Yan, C. Xie, J. Huang, Z. Ren, X. Li, S. Best, X. Cai and G. Han, *Nanoscale*, 2018, 13423–13442.

195 X. Zhao, K. C. Zhao, L. J. Chen, Y. S. Liu, J. L. Liu and X. P. Yan, *Chem. Sci.*, 2020, **12**, 442–452.

196 T. Lecuyer, M. A. Durand, J. Volatron, M. Desmau, R. Lai-Kuen, Y. Corvis, J. Seguin, G. Wang, D. Alloyeau, D. Scherman, N. Mignet, F. Gazeau and C. Richard, *Nanoscale*, 2020, **12**, 1967–1974.